

Site-specific dehydration of olivines from San Carlos and Kilauea Iki

Introduction

The diffusivity of hydrogen in olivine is a fundamental physical quantity critical for understanding a wide range of earth and planetary processes, most notably for understanding the deep water cycle. Water can affect global-scale phenomenon such as melting relations and strength, and so in turn may control mantle rheology and the occurrence of plate tectonics (Keppler and Smyth 2006; Bell and Rossman 1992). Accurate knowledge of the diffusivities also has great potential to serve as a chronometer to determine magma ascent times from hydrogen diffusion profiles in olivine phenocrysts.

Hydrogen may be incorporated into the olivine lattice in a variety of ways that can be distinguished by differences in the absorbances of O-H bonds (Berry et al. 2005; Ingrin et al. 2013). Broadly, H incorporation mechanisms fall into two categories: relatively high wavenumber peaks produced associated with silicon vacancies and relatively low wavenumber peaks associated with magnesium vacancies. A doublet of peaks at 3525 and 3573 cm⁻¹ has been linked to the presence of 2 H⁺ ions, a Si⁴⁺ vacancy, and Ti⁴⁺ on the metal site (Berry et al. 2007). This mechanism, labeled [Ti], has been suggested to control mantle rheology (Faul et al. 2016). Multiple other high wavenumber peaks (3450-3620 cm⁻¹) represent 4 H⁺ ions charge-balanced by a Si⁴⁺ vacancy and are labeled [Si]. Some lower wavenumber peaks (3300-3400 cm⁻¹) appear when a Mg²⁺ vacancy is charge-balanced by a H⁺ and a trivalent cation on a Mg²⁺ site (Blanchard et al. 2017), and these are labeled [tri]. Low wavenumber peaks between 3200 and 3250 cm⁻¹ have been associated with 2 H⁺ charge-balancing a Mg²⁺ vacancy, and these are labeled [Mg]. The different mechanisms are important because the rate at which H moves through the lattice may depend at least in part on its incorporation mechanism (Padrón-Navarta, Hermann, and O'Neill 2014).

More about usage and background, H incorporation mechanisms, previous diffusivity measurements...

Some background about Kiki and SC. Helz paper: Kiki QMF+1/2 or so.

Experimental methods

We provide, for the first time, time-series data showing water loss from the same single crystal of Fe-bearing olivine. We do this for two olivines: partially hydrated xenolithic olivine from San Carlos and phenocrysts from Kilauea Iki.

Sample selection and preparation

Olivines from San Carlos, AZ and Kilauea Iki were chemically characterized and used for H diffusion experiments. The San Carlos olivine similar to that used in previous hydration experiments (Mackwell and Kohlstedt 1990; Kohlstedt and Mackwell 1998) was provided by David Kohlstedt. Here we extend that work by examining site-specific dehydration behavior. The Kilauea Iki olivines were collected from scoria from the 1959 Episode 1 eruption of Kilauea Iki and have been described in detail by David Ferguson (Ferguson et al. 2016), who provided the samples. The Kilauea Iki samples are of great interest because they provide the first direct experimental measurements of H diffusion in all 3 crystallographic directions of inclusion-free olivine phenocrysts.

A large crack and inclusion-free piece of San Carlos olivine, SC1 (IGSN: IEFERSCO1), was oriented by Laue camera at Cornell University and then cut into a series of smaller pieces approximately 2-3 mm long on each side using a diamond saw. One of the resulting sub-pieces, SC1-1 (IGSN: IEFERJAI3), was polished with 0.25 μm diamond paste and used to estimate the initial water concentration by FTIR. Additional pieces of SC1 were used to test the hydration procedure, and pieces SC1-7 (IGSN: IEFERJAI9) and SC1-2 (IGSN: IEFERJAI4) were partially hydrated and then polished with 0.25 μm diamond paste for FTIR. SC1-2 was then sequentially dehydrated with FTIR profiles measured after each dehydration step and afterwards analyzed by EMPA and SIMS.

A large, relatively clear piece of the Kilauea Iki olivine, Kiki (IGSN: IEFERJAIC), was oriented based on morphology and polished into a block shape of dimensions $2 \times 1 \times 1.3$ mm. The orientations were then confirmed by electron backscatter diffraction (EBSD) at the American Museum on Natural History (AMNH). The untreated Kiki sample was characterized by EMPA, SIMS, and polarized FTIR prior to dehydration. The sample was initially zoned in hydrogen, and the low hydrogen rims were polished off to create a homogeneous initial block.

Sample thicknesses in all three directions were measured with a digital micrometer accurate to within $\pm 5 \mu\text{m}$. Additional details for all samples, including images and sample dimensions, are available online at geosamples.org.

Electron microprobe analysis

Major elements of SC1-2 and Kiki were analyzed by electron microprobe at AMNH along traverses parallel to those on which water measurements were made to confirm homogeneity of the samples. The beam current was 20 nA, and the accelerating voltage was 15 kV.

Initial water concentrations

The initial water concentration in each olivine was estimated using both polarized FTIR and SIMS. Polarized FTIR measurements were performed at AMNH using the Thermo Nicolet Nexus 670 infrared spectrometer and Thermo Nicolet Continuum 15 \times infrared microscope with a resolution of 4 cm^{-1} , spot sizes of $100 \times 100 \mu\text{m}$, an average of 200 scans, and a ZnSe polarizer. Initial water concentrations were estimated from 3 orthogonal polarized measurements (Libowitzky and Rossman 1996; Shuai and Yang 2017) by applying the Bell and Withers calibrations (Bell et al. 2003; Withers et al. 2012). To account for the large error associated with baseline choice, 3 different baselines were drawn, and the resulting areas were averaged. Traverses along all three directions did not show significant zonation in bulk or peak-specific water in the untreated samples.

Erik Hauri measured the C, H, F, P, and Cl concentrations by nanoSIMS along traverses parallel to [001] in SC1-2 and parallel to [010] in Kiki as part of the CIDER workshop on electrical conductivity in hydrous olivine. SIMS measurements were made before Kiki was dehydrated but after the final dehydration heating step for SC1-2. The area under the O-H stretching peaks with the electric vector E || [100] is equal to that of both the untreated SC1-1 ($7 \pm 5 \text{ cm}^{-2}$) and of the partially hydrated and then dehydrated SC1-2 ($7 \pm 6 \text{ cm}^{-2}$). Therefore, the SIMS measurements of the hydrated and then dehydrated SC1-2 were taken as a reasonable estimate of the initial water concentration in SC1.

Hydration of San Carlos olivine

Two pieces of previously oriented San Carlos olivine SC1, SC1-7 and SC1-2, were partially hydrated in a $\frac{3}{4}$ " Boyd-type piston cylinder apparatus with a BaCO₃ pressure medium using a procedure broadly similar to that of Jollands et al. (2016). Here the samples were placed in copper capsules and surrounded by liquid distilled H₂O and a powdered mixture of Ni and NiO to control oxygen fugacity and San Carlos olivine and enstatite to control silica activity (Figure 1). Temperatures were controlled with a D-type

(W3%Re-W25%Re) with control precision of $\pm 2^\circ\text{C}$ and probable accuracy of $\pm 20^\circ\text{C}$. After rapid quenching followed by relatively slow decompression, the capsules were pierced with a drill to confirm water was still present and then dissolved overnight in a mixture of 1:1 H_2O to HNO_3 . The rectangular parallelepiped samples were then mounted in CrystalBond, polished with 0.25 μm diamond paste on all sides, and cleaned in acetone.

SC1-7 was heated for 7 hours at 10 kbar and temperature readings of 1000°C, but the experiment ended when capsule began to melt, suggesting the true temperature in the capsule was closer to 1085°C, the melting point of copper or, more likely, the Cu was contaminated, perhaps with a small amount of oxygen, resulting in freezing point depression. This temperature range and pressure correspond to water fugacities of 1.9-2.0 GPa (Withers 2013). Within this temperature range, given the dimensions of the sample and the diffusivities reported by Kohlstedt and Mackwell (1998), the experiment time of 7 hours should allow the completion of proton-polaron diffusion and enter into the stage of diffusion dominated by the slower proton-vacancy mechanism without fully saturating the sample. This experiment allows a direct comparison with previous work (Kohlstedt and Mackwell 1998; Demouchy and Mackwell 2006).

To more thoroughly understand the transition between proton-polaron-dominated diffusion and pure proton-vacancy diffusion, SC1-2 was hydrated at a nominal temperature of 800 °C and 10 kbar pressure, which corresponds to a water fugacity of 1.6 GPa (Withers 2013), for 17.5 hours. That time was chosen in order to reach, but not pass, what Kohlstedt and Mackwell (1998) call “metastable equilibrium”, the point at which all of the initial Fe^{3+} is reduced as H^+ diffuses into the sample following the proton-polaron mechanism. If the model used by Kohlstedt and Mackwell (1998) is correct, the hydrogen concentration in SC1-2 after the piston cylinder experiment should be homogeneous, and the concentration should be lower than the true solubility and presumably determined by the initial concentration of ferric iron. If the “metastable equilibrium” hydrogen concentration is both large enough to easily measure and homogeneous, then SC1-2 is a suitable starting material for step-wise dehydration experiments.

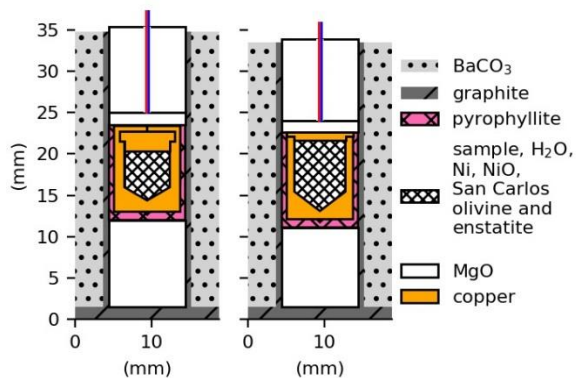


Figure 1. Schematic cross-sections illustrating the experimental design for hydrating San Carlos olivine samples SC1-2 and SC1-7 in a piston cylinder apparatus showing the BaCO_3 pressure medium, graphite furnace and pyrophyllite sleeve surrounding an unwelded copper capsule containing the sample, liquid water, and a powdered mixture of nickel, nickel oxide, San Carlos olivine, and San Carlos enstatite. The sleeve and capsule are supported by MgO , and D-type W-Re thermocouples (colored lines) extend through cylindrical holes in the MgO .

Dehydration

Olivine samples SC1-2 (the same sample that was partially hydrated according to the procedure described above) and Kiki (untreated) were dehydrated in increments using the vertical furnace used in

previous dehydration experiments (Ferriss 2015), and oxygen fugacity was controlled with a mixture of CO and CO₂. The partially hydrated sample SC1-2 was heated at 800 °C for 1, 3, 7, 13, 19, 43, and 68 hours at an oxygen fugacity 10^{-16.5} bars, equivalent to NNO-2.6, where NNO is the nickel-nickel oxide buffer. Kiki was heated at 800°C for 1 and 8 hours; then 3, 6, 7, and 8 hours at 1000°C. All heating steps for Kiki were conducted at oxygen fugacity of NNO-2.6 except for the final step at 1000°C, which was conducted at relatively oxidizing conditions, NNO+2.

FTIR and diffusion modeling

Before heat treatment and in between each heating step, samples were analyzed by polarized FTIR along 3 orthogonal traverses parallel to the three crystallographic directions in the uncut crystal. These analyses use the same conditions described above for estimating the initial water and were in all cases conducted with polarized radiation with the electric vector E || [100]. Quadratic baselines were drawn based on the curve of the spectrum of the untreated and/or the dehydrated sample, with typical wavenumber ranges of 3200–3700 cm⁻¹, and the resulting areas were scaled up to approximate hydrogen concentrations by comparison with the corresponding area measured in the same way in the untreated sample, for which hydrogen concentrations are known.

Each profile was normalized to the initial measurements to produce a ratio of the final to initial area A/A₀ and scaled up to a true concentration based on the initial concentrations, A₀, determined above. These “whole-block” concentrations represent the average concentration through the entire path of the infrared beam, and the forward models used to determine hydrogen diffusivities in each direction are modified accordingly following the models described in E. Ferriss et al. (2015) and Elizabeth Ferriss, Plank, and Walker (2016) and implemented using the free, open-source software package pynams (Ferriss 2015).

To explore possible differences among various hydrogen incorporation mechanisms, the same normalization and fitting procedures were applied to individual peaks using the peak heights relative to the quadratic baseline. Particular emphasis was placed on peaks at the following 4 wavenumbers: 3600, 3525, 3356, and 3236 cm⁻¹. The peak at 3600 cm⁻¹, designated [Si-Fe²⁺], is most likely 4H⁺ in a Si⁴⁺ vacancy with a nearby Fe²⁺ (Blanchard et al. 2017). The peak at 3525 cm⁻¹, designated [Ti-3525], is one of two prominent peaks produced by 2H⁺ coupled with a Si⁴⁺ vacancy and a Ti⁴⁺ on a metal site. We focus on this peak both to minimize interferences with nearby [Si] peaks and to more directly compare with the results of Padrón-Navarta, Hermann, and O’Neill (2014). The 3356 cm⁻¹ peak, designated [tri-Fe³⁺-3356], is the most prominent peak in a doublet associated with a Mg²⁺ vacancy charge-balanced by H⁺ and Fe³⁺ substituting on a metal site (Blanchard et al. 2017), and the 3236 cm⁻¹, designated [Mg], is likely 2H⁺ charge-balanced by a Mg²⁺ vacancy (Berry et al. 2005).

All of the raw FTIR spectra, baselines, and computer code used to produce all calculations and figures reported in this paper will be made available on GitHub.

Results

Characterization of the starting material

Microprobe analysis did not reveal any significant zonation along the measured profiles and were generally consistent with previous work (Ruprecht and Plank 2013; Ferguson et al. 2016) with somewhat lower forsterite numbers: 87.7±0.2 in SC1-2 and 86.2±0.2 in Kiki. The San Carlos olivine used in previous H diffusion experiments had a reported approximate composition with forsterite number 91 (Mackwell and Kohlstedt 1990).

The initial water concentration was estimated from the polarized FTIR measurements and baselines shown in Figure 2 using both the Bell calibration and the Withers calibration and also by nanoSIMS

(Table 1). These three estimates were averaged to produce initial water concentration estimates of 15 ± 2 ppm H₂O in the Kilauea Iki olivine and 4 ± 1 ppm H₂O in the San Carlos olivine. These low concentrations are consistent with previous work on San Carlos olivine (Peslier and Luhr 2006; Kurosawa, Yurimoto, and Sueno 1997). The hydrogen concentration in the Kilauea Iki sample, for which the low rims had been polished off to prepare the sample as a rectangular parallelepiped, was homogeneous by both SIMS and FTIR.

Several different O-H peaks were observed in the initial materials. The prominent peaks at wavenumbers 3525 and 3573 cm⁻¹ oriented primarily || [100] in both Kilauea Iki and San Carlos olivine correspond to the [Ti] incorporation mechanism, and the high-wavenumber peaks that primarily appear as shoulders on the [Ti] peaks correspond to the [Si] mechanism (Berry et al. 2005). A very small peak at 3600 cm⁻¹ present in both samples has been ascribed to [Si] with nearby Fe²⁺ (Blanchard et al. 2017). Because of the association with Fe²⁺, we label this peak [Si-Fe²⁺]. The Kilauea Iki olivine, but not the untreated San Carlos olivine, contains prominent [tri] peaks. These peaks at 3356 and 3329 cm⁻¹ correspond exactly to the peak locations that Blanchard et al. (2017) associate with Fe³⁺, and which we therefore designate.

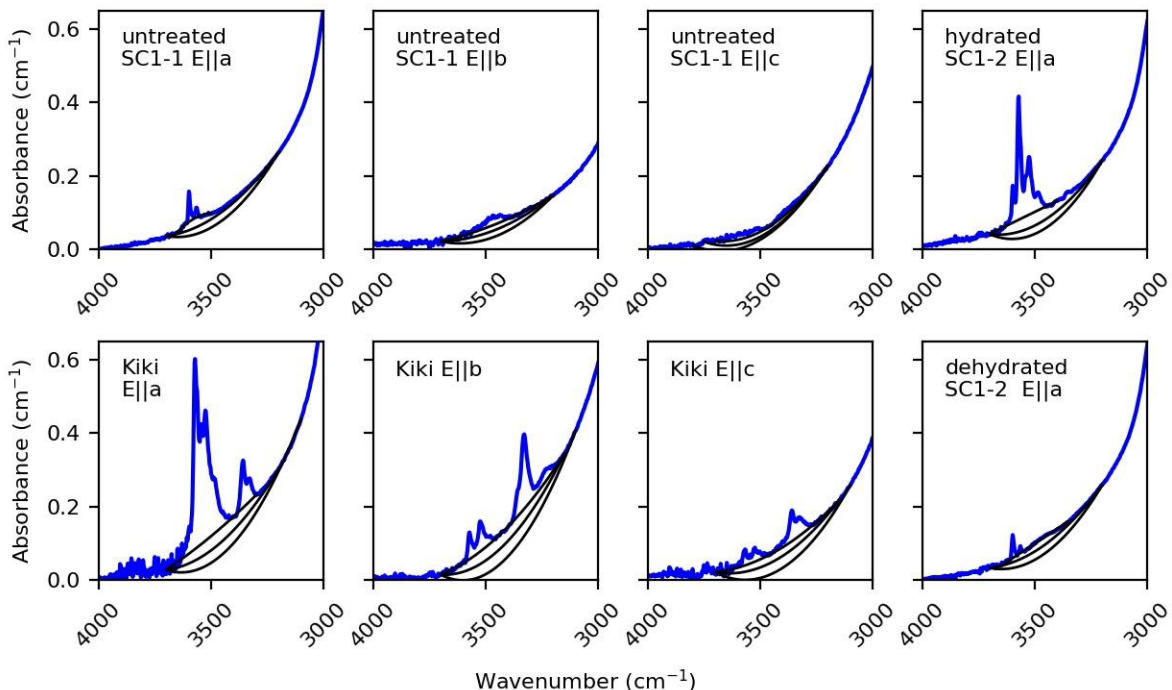


Figure 2. Polarized FTIR spectra (thick blue) and baselines (black) used to estimate the water concentrations of Kilauea Iki olivine (Kiki) and San Carlos olivine (SC1-1 and SC1-2) reported in Table 1.

Table 1. Water concentration estimates for Kilauea Iki olivine and San Carlos olivine based on polarized FTIR areas (Figure 2 and Figure 3) and SIMS measurements.

	Kilauea Iki olivine; Kiki	San Carlos olivine; sub-samples of SC1	
FTIR area E [100] (cm ⁻²)	52+/-10	7+/-5 55+/-17 24+/-8	untreated SC1-1 partially hydrated SC1-7 partially hydrated SC1-2

		7+/-6	dehydrated SC1-2
FTIR area E [010] (cm ⁻²)	31+/-13	8+/-5	untreated SC1-1
FTIR area E [001] (cm ⁻²)	18+/-9	9+/-4	untreated SC1-1
FTIR area summed over 3 directions (cm ⁻²)	101+/-19	24+/-8	untreated SC1-1
Water, Bell calibration (ppm H ₂ O)	19+/-4	4.5+/-1.5	untreated SC1-1
Water, Withers calibration (ppm H ₂ O)	12+/-2	3+/-1	untreated SC1-1
Water, SIMS (ppm H ₂ O)	14+/-1	5+1	dehydrated SC1-2
Average initial water (ppm H ₂ O)	15+/-2	4+/-1	SC1
Ratio of water in ppm H ₂ O to area in cm ⁻² with E [100]	0.3	0.6	SC1-1
Average water (ppm H ₂ O) after piston cylinder experiment	Not treated with pressure	32+/-23 14+/-10	partially hydrated SC1-7 partially hydrated SC1-2

Hydration

Changes in FTIR absorbance indicate that hydrogen was successfully incorporated into San Carlos olivine samples SC1-7 and SC1-2 (Figure 3A). To construct hydrogen profiles, quadratic baselines (Figure 3B and C) were drawn to match both the curve of the spectrum of the untreated sample and the middle baselines used to determine the initial water concentration in Figure 2. The area under each curve was determined and scaled to an estimated H concentration by multiplying by 0.6, following the ratio of concentration to area with E || [100] reported for San Carlos olivine in Table 1.

The partially hydrated sample SC1-2 was sufficiently homogeneous for both bulk H and individual peaks to serve as a reasonable starting material for subsequent dehydration experiments (Figure 4). If we ignore the uncertainties associated with baseline choice and use only the quadratic baseline shown in Figure 3C, the water concentration across hydrated SC1-2 is 15±1 ppm H₂O. Although there is a small increase in area around the [tri] peaks, the large majority of the hydrogen in the hydrated SC1-2 is incorporated as [Ti] and [Si], and these profiles are also homogeneous.

In contrast, hydrogen zonation in SC1-7 is clearly observed, with water concentrations of 38±7 ppm H₂O using the quadratic baseline shown in Figure 3B. The variations in concentration are most apparent || [001], consistent with previously work showing c as fast direction during proton-vacancy mechanism diffusion (Kohlstedt and Mackwell 1998; Demouchy and Mackwell 2006).

Quantifying the diffusivities in SC1-7 requires major assumptions about both the solubility and ‘metastable equilibrium’ concentrations. The estimated concentration of 58 ppm H₂O on the edge of SC1-7 is much lower than the expected final solubility of around 112 ppm H₂O (Mosenfelder et al. 2006), and the ‘metastable equilibrium’ concentration of 15±1 ppm H₂O is much higher than the 0.4 ppm H₂O (7 H/10⁶Si) reported by Kohlstedt and Mackwell (1998). Kohlstedt and Mackwell (1998) also report a final concentration of only 3 ppm H₂O (50 H/10⁶Si), suggesting that the scaling factor used is significantly different among studies. If Kohlstedt and Mackwell (1998)’s final concentration is assumed to be 112 ppm H₂O, then the scaled-up “metastable equilibrium” concentration would be 16 ppm H₂O, very close to what is observed in SC1-2. Path-integrated 3D diffusion modeling that assumes an initial “metastable equilibrium” concentration of 15 ppm H₂O, a final solubility concentration of 112 ppm H₂O, and the diffusivities expected at 1000°C for the proton-vacancy diffusion mechanism (Kohlstedt and Mackwell 1998) provides a reasonably close match to the measured data for bulk H and the [Ti] peak (Figure 4). The [Si-Fe²⁺] peak is somewhat slower, and the [tri-Fe³⁺-3356] and [Mg] peaks are somewhat faster. Least-squares fitting to the data without any constraints often gave results that varied by several orders of magnitude in a given direction from one set of profile to another and typically had very large errors,

so to get more quantitative sense of the difference in diffusivities, we held all variables constant like those shown in Figure 4 and then varied the diffusivity || c (Figure 4 orange lines). The resulting diffusivities || c are as follows: $10^{-11.8 \pm 1.6} \text{ m}^2/\text{s}$ for bulk H, $10^{-12.2 \pm 20.3} \text{ m}^2/\text{s}$ for [Si-Fe²⁺], $10^{-12.0 \pm 5.2} \text{ m}^2/\text{s}$ for [Ti], $10^{-11.7 \pm 2.7} \text{ m}^2/\text{s}$ for [tri-Fe³⁺-3356], and $10^{-11.4 \pm 0.6} \text{ m}^2/\text{s}$ for [Mg]. These differences in diffusivities are in general agreement with the observation that [Si] moves more slowly than [Ti], which moves more slowly than [Mg] in forsterite (Padrón-Navarta, Hermann, and O'Neill 2014), although all of these peaks are changing significantly more quickly in these experiments than in the synthetic, Fe-free forsterite used by Padrón-Navarta, Hermann, and O'Neill (2014) (Figure 5).

To Do

Model Iki 1000C with 98% pp; put on Fig 5

Cite new Tolland – move solubilities

Model 2 rates thing (incremental + change initial to average of previous step, possibly weight middle) during dehydration of SC1-2

Standard Arrhenius plots – plot everything and see

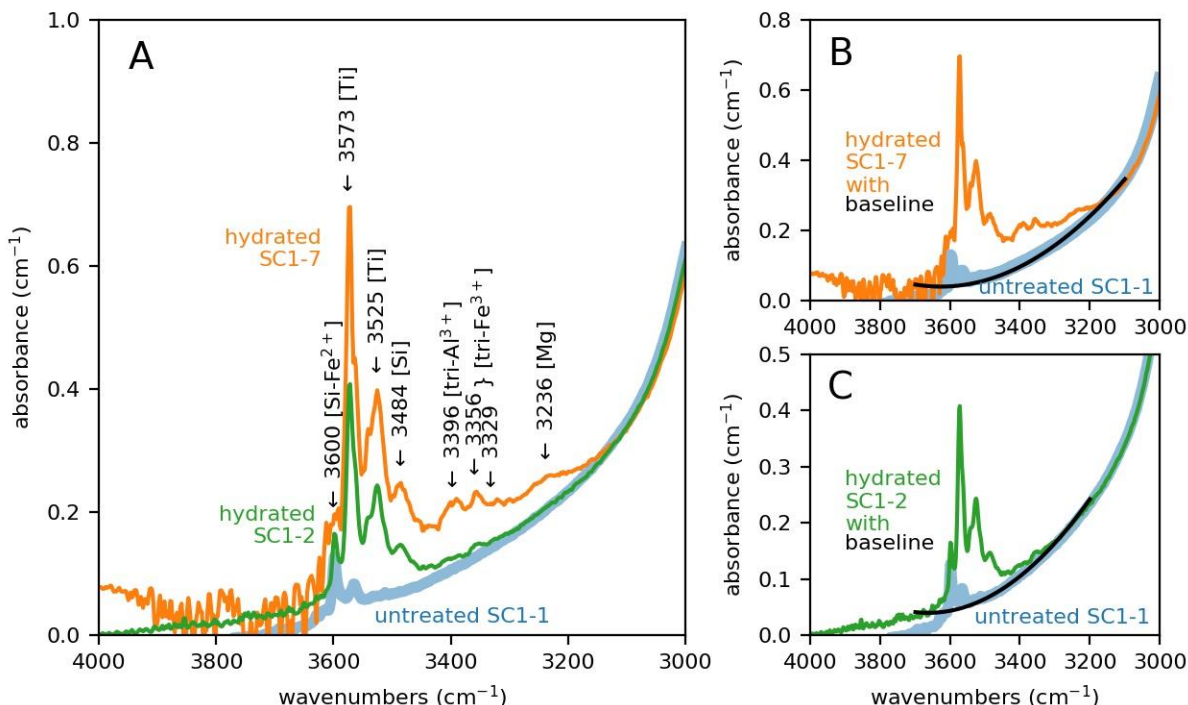


Figure 3. (A) Polarized FTIR spectra with electric vector E || [100] averaged across all traverses in three directions of San Carlos olivine SC1 pieces that were untreated (SC1-1, blue); hydrated in a piston cylinder for exactly the amount of time needed to reach “metastable equilibrium” by the proton-polaron mechanism (SC1-2, green) at 800°C; and hydrated long enough to enter into proton-vacancy-dominated diffusion without saturating the sample (SC1-7, orange) with major peaks labeled. The shapes of the quadratic baselines used to calculate the areas under each curve for spectra measured are shown for SC1-7 (B) and SC1-2 (C). Note the differences in the y-axis scale.

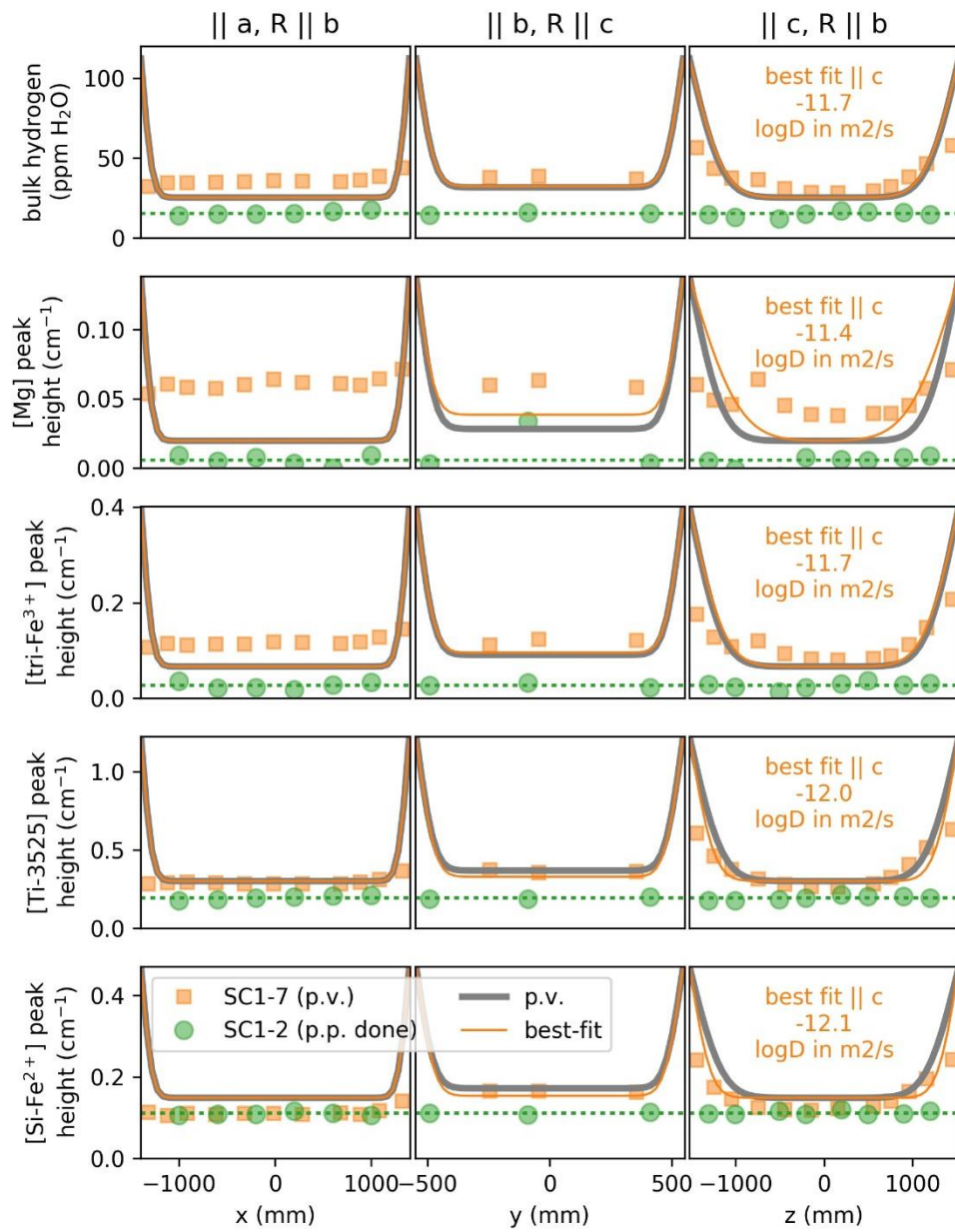


Figure 4. Concentration profiles across San Carlos olivine samples SC1-2 and SC1-7 after partial hydration in a piston cylinder as measured through the uncut block. R is the ray path of the infrared beam, and the electric vector E of the polarized infrared beam is in all cases \parallel a. Hydrogen concentrations are estimated from polarized FTIR spectra based using the areas under the baselines shown in Figure 3 and initial hydrogen contents from Table 1. Profiles constructed with alternative baselines are provided in Supplementary Figure 2 and Supplementary Figure 3. Grey curves show the expected diffusion curves based on the diffusivities (D) for the proton-vacancy (p.v.) mechanism diffusion at 1000°C ($D_{\parallel a} = 10^{-12.8} \text{ m}^2/\text{s}$; $D_{\parallel b} = -10^{-13.2} \text{ m}^2/\text{s}$; $D_{\parallel c} = 10^{-11.8} \text{ m}^2/\text{s}$), an initial “metastable equilibrium” concentration equal to the mean concentration or peak height in the hydrated SC1-2 (dotted green lines, where all diffusion possible by the proton-polaron, or p.p., mechanism has been completed) and final concentration equal to the expected solubility of 112 ppm H_2O . Thin orange lines show estimated diffusivities changed \parallel c to better fit the data.

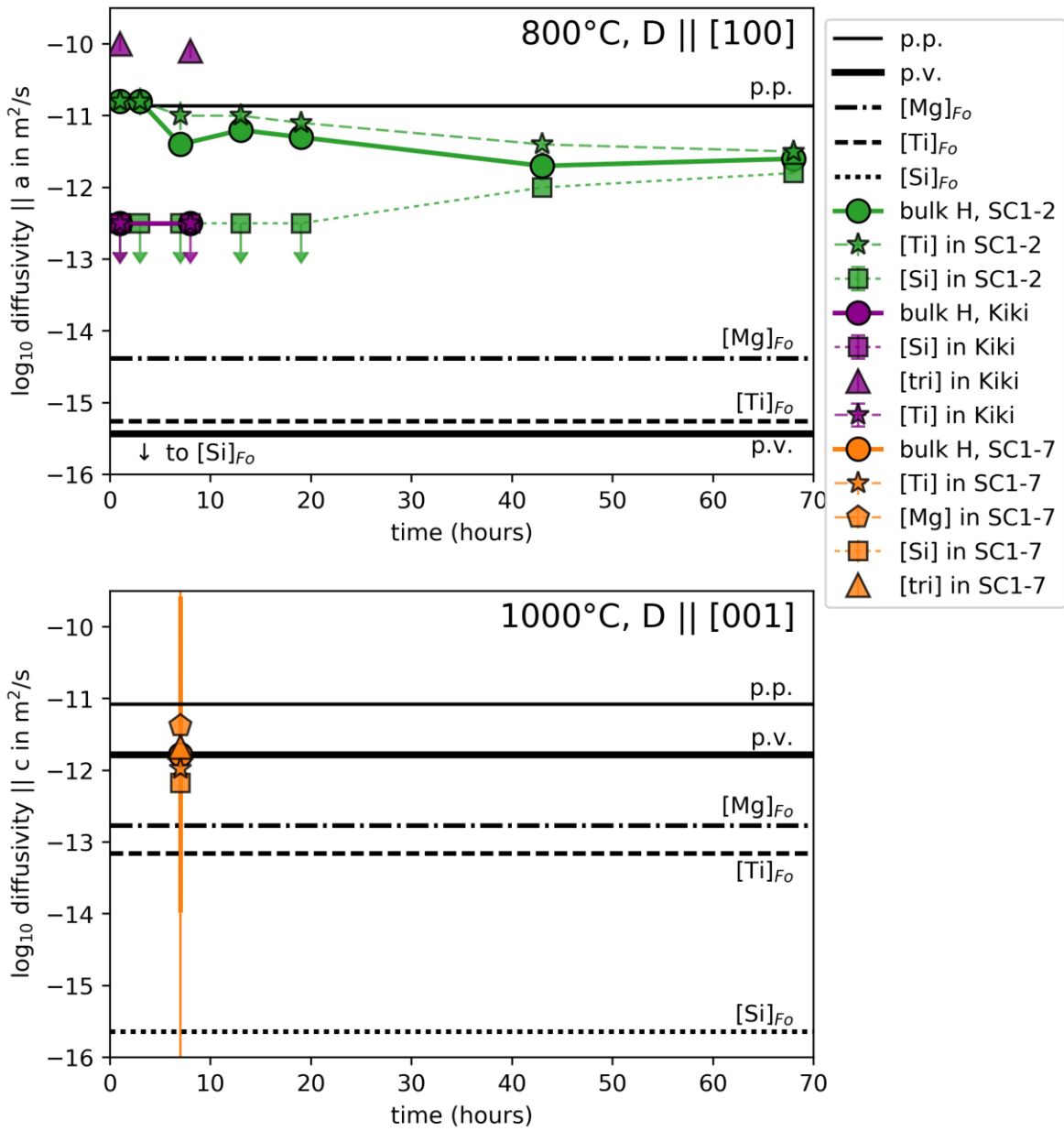


Figure 5. Diffusivities (D) determined at two different temperatures, 800 and 1000°C, during hydration of San Carlos olivine SC1-7 primarily by the proton-vacancy or “p.v.” mechanism at 1000°C, dehydration of San Carlos olivine SC1-2 after partial hydration by the proton-polaron or “p.p.” mechanism at 800°C, and dehydration of Kilauea Iki olivine Kiki first at 800°C and then 1000°C (COMING SOON) compared with expected diffusivities for bulk H (Kohlstedt and Mackwell 1998) and peak-specific H incorporation mechanisms $[Ti]$, $[Mg]$, $[Si]$, and $[tri]$ in unoriented synthetic forsterite (Fo) (Padrón-Navarta, Hermann, and O’Neill 2014). Note diffusivities $\parallel [100]$, the fast direction in the p.p., are plotted in the 800°C panel, and diffusivities $\parallel [001]$, the fast direction in p.v., are plotted in the 1000°C panel. **Data and associated errors are reported in Table X.** Note that many of the data points, particularly for the early stages of dehydration of SC1-2 are poorly constrained and so have very large reported errors that are not plotted here for clarity.

Dehydration

SC1-2 and Kiki, two homogeneous blocks of olivine with similar initial starting hydrogen concentrations but very different histories and compositions and distributions of hydrogen, were sequentially dehydrated in a gas-mixing furnace (Figure 6). Quadratic baselines were used to construct water loss profiles (Figure 7, Figure 8). These profiles were normalized to the initial hydrated concentrations. Several of the profiles are assymetric, which we attribute primarily to error in the quadratic baselines used. Linear baselines drawn between wavenumbers 3700 and 3200 cm⁻¹ remove much of this asymmetry (Supplementary Figure 4) but could in some cases result in negative areas, particularly during the final dehydration steps and near edges (Supplementary Figure 5). Path-integrated 3-dimensional diffusion modeling was performed to estimate the rate of hydrogen movement for each time step in SC1-2 (Supplementary Figure 6 through Supplementary Figure 12) and Kiki (**COMING SOON**), and the results are shown in Figure 5.

We determined diffusivities for bulk H, [Si-Fe²⁺] at 3600 cm⁻¹, and [Ti-3525] in San Carlos SC1-2. The other [Ti] peak and [Si] peaks profiles in SC1-2 are similar to [Ti-3525]. The [Si-Fe²⁺] peak is clearly slower than the rest of the peaks and was essentially immobile for the first 5 heating steps. After 43 hours, when the large majority of the initial H had left the crystal and the bulk of the remaining H was present in the [Si-Fe²⁺] peak, clear H-loss profiles could be observed, with apparent diffusivities that were relatively fast compared to the initial stages and with a fast direction || a. These [Si-Fe²⁺] loss profiles also differ from the majority of profiles observed in this study in that they did not appear to be going to zero near the edges, but rather to about 40% of the initial, which was the final concentration used when modeling the diffusivities. Because this peak does not go to zero, the bulk H also cannot go to zero. Consequently, the final bulk H concentration was modeled as 15% of the initial homogeneous partially hydrated concentration.

While the [Si-Fe²⁺] peak sped up, the [Ti-3525] peak began slowing down after about 7 hours. To observe this, compare the close correspondance of the [Ti-3525] data with the expected proton-polaron curves after 7 hours (Supplementary Figure 8) with the increasing difference between the two in subsequent time-steps. The two mechanisms eventually come close to converging, but the [Ti-3525] peak is always slightly faster. Some disordered [tri] peaks were also occasionally observed near the edge of SC1-2 (Supplementary Figure 5), but these were so uncommon that they are difficult to use to obtain diffusivities.

Experimentation on the Kilauea Iki sample took place in multiple stages. First, the sample was treated exactly the same way as SC1-2 during dehydration: heated for 1 and then a total of 8 hours at 800°C in a gas-mixing furnace at QFM-2. This procedure resulted in some redistribution of the H, primarily from [tri-Fe³⁺] to [Si] (Figure 8), but did not produce clear H loss in bulk H like what was observed in the partially hydrated SC1-2 treated the same way. The difference between the two olivines is most apparent in the comparison between clear loss in the [Ti-3525] peak from SC1-2 after 7 hours of heating at 800°C (Supplementary Figure 8) compared to essentially no movement of the same peak in the similarly-sized Kilauea Iki sample after 8 hours of heating at the same temperature and oxygen fugacity (Supplementary Figure 14). The rate of loss from the [tri-Fe³⁺] peak could be quantified from the loss profiles following the same procedure used for SC1-2 of starting with the expected proton-polaron mechanism diffusivities and allowing the diffusivity to change || a. The results are 10^{-10.0±0.1} m²/s at 1 hour and 10^{-10.1±0.1} m²/s at 8 hours.

During dehydration of the Kilauea Iki sample at 800°C, clear profiles could be distinguished for [tri- Fe^{3+} -3356] as well as the two peaks [Ti-3525] and [Si- Fe^{2+}] discussed for SC1-2.

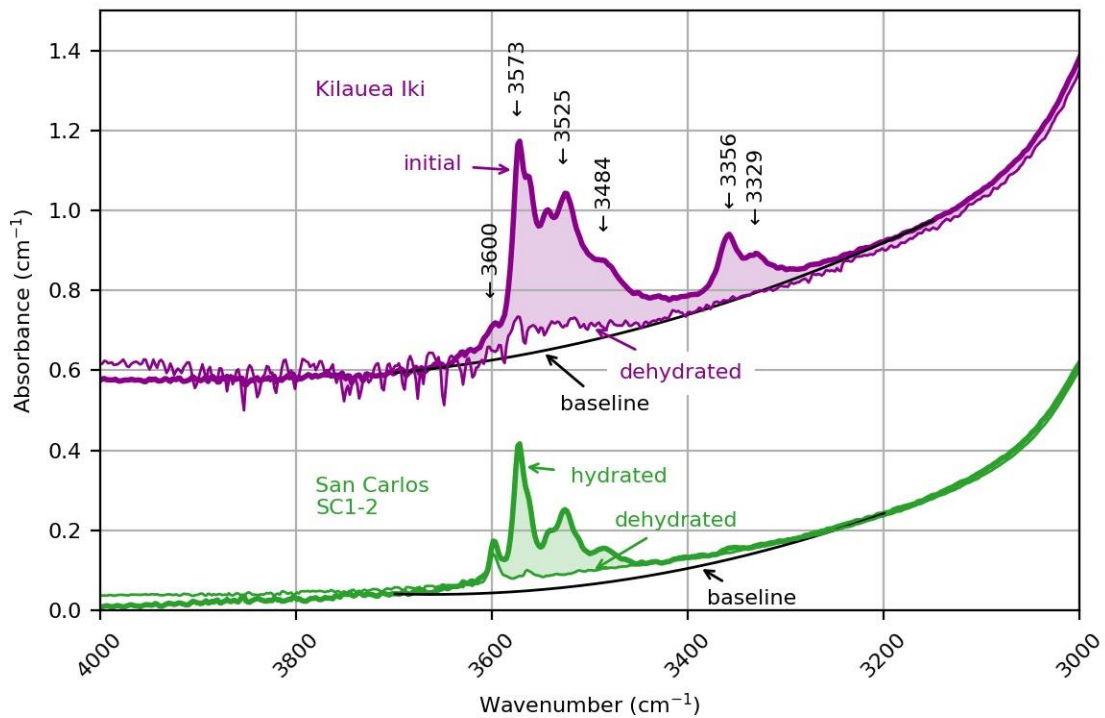


Figure 6. Averaged polarized FTIR spectra with electric vector $E \parallel [100]$ of untreated Kilauea Iki olivine Kiki (offset for clarity) and partially hydrated San Carlos olivine SC1-2. Both samples contain around 15 ppm H_2O (Table 1), but the hydrogen is incorporated into the structures in different ways, resulting in different peak locations and absorbances $\parallel [100]$. Quadratic baselines like those shown in black were used to construct hydrogen loss profiles.

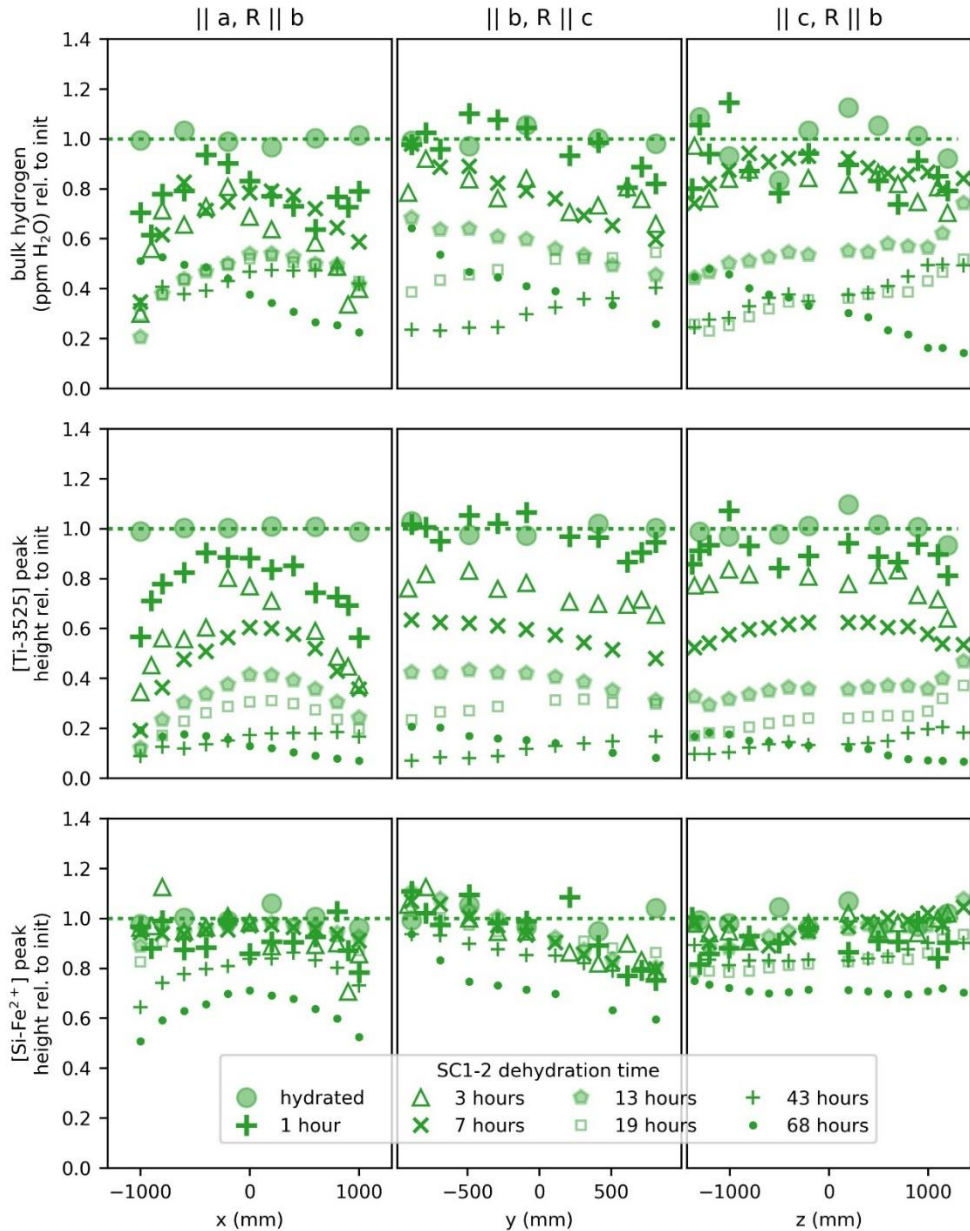


Figure 7. Profiles of bulk H (top) and two peaks during step-wise dehydration of partially hydrated San Carlos olivine SC1-2 at 1 atm, 800°C, and QFM-2. The bulk H is scaled assuming that the hydrated sample contained 14 ppm H₂O (Table 1), and all profiles are normalized relative to the hydrated profile to account for small amounts of initial zonation. We attribute the asymmetry in some of the profiles primarily to differences between the baselines used to determine these areas (Figure 6) and the true baselines, which could not be easily determined and also appeared to change over time.

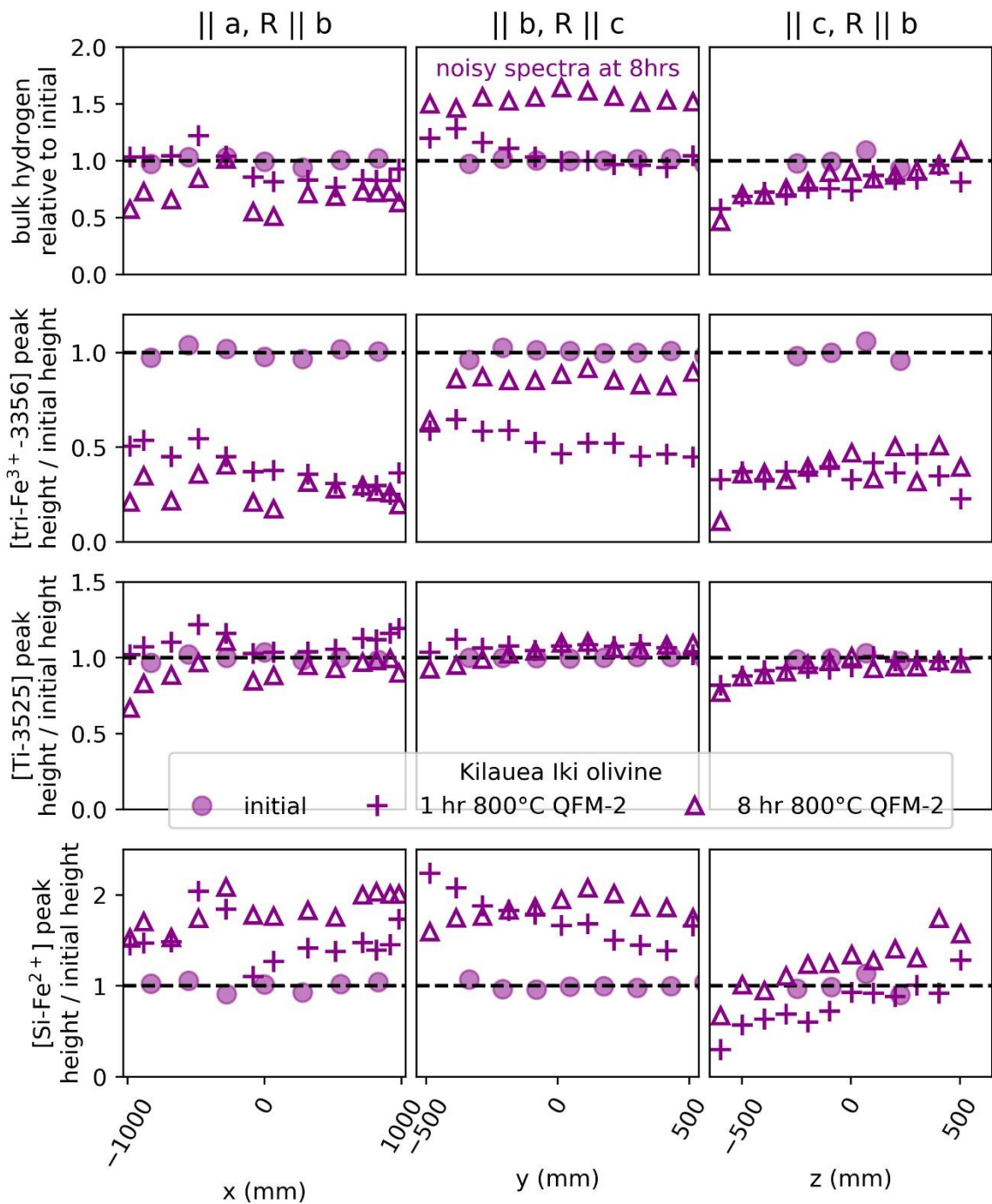
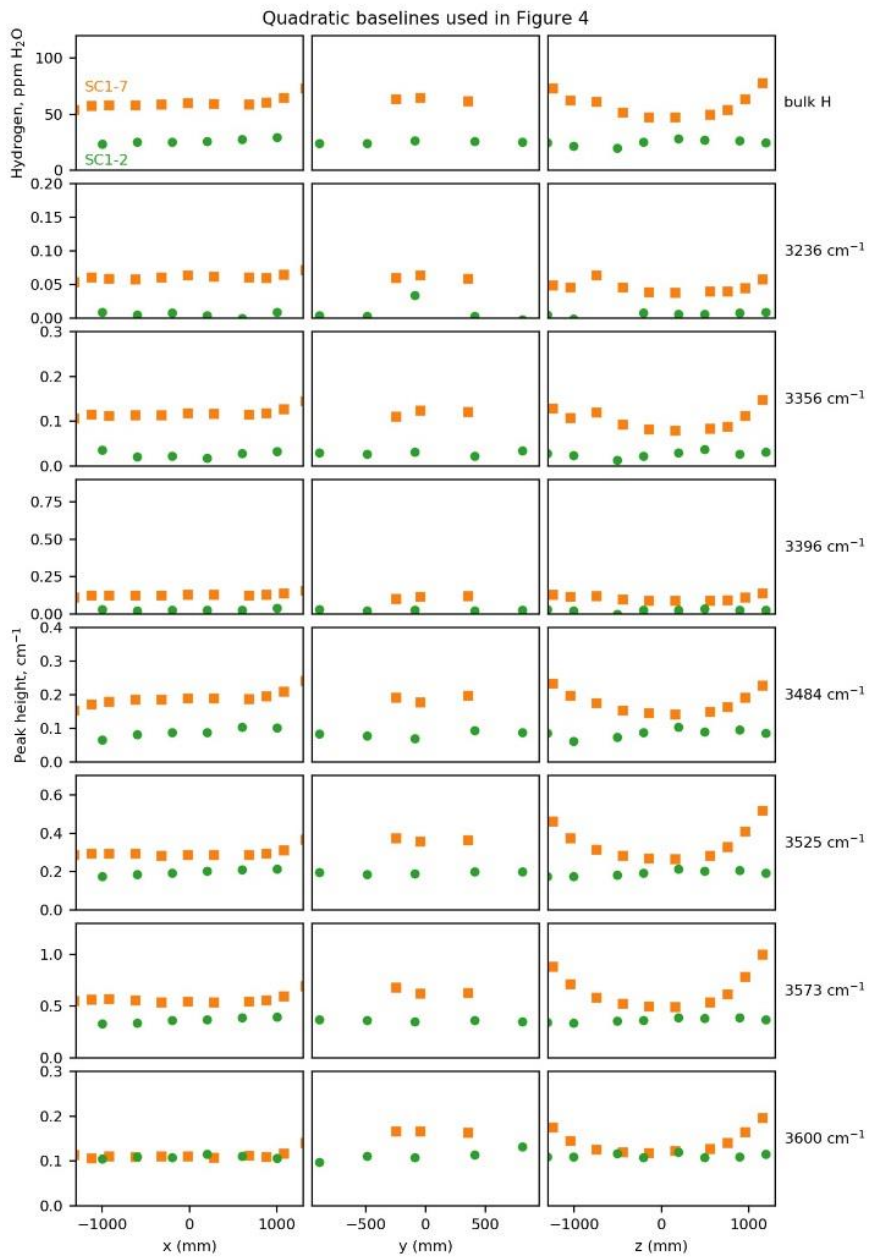
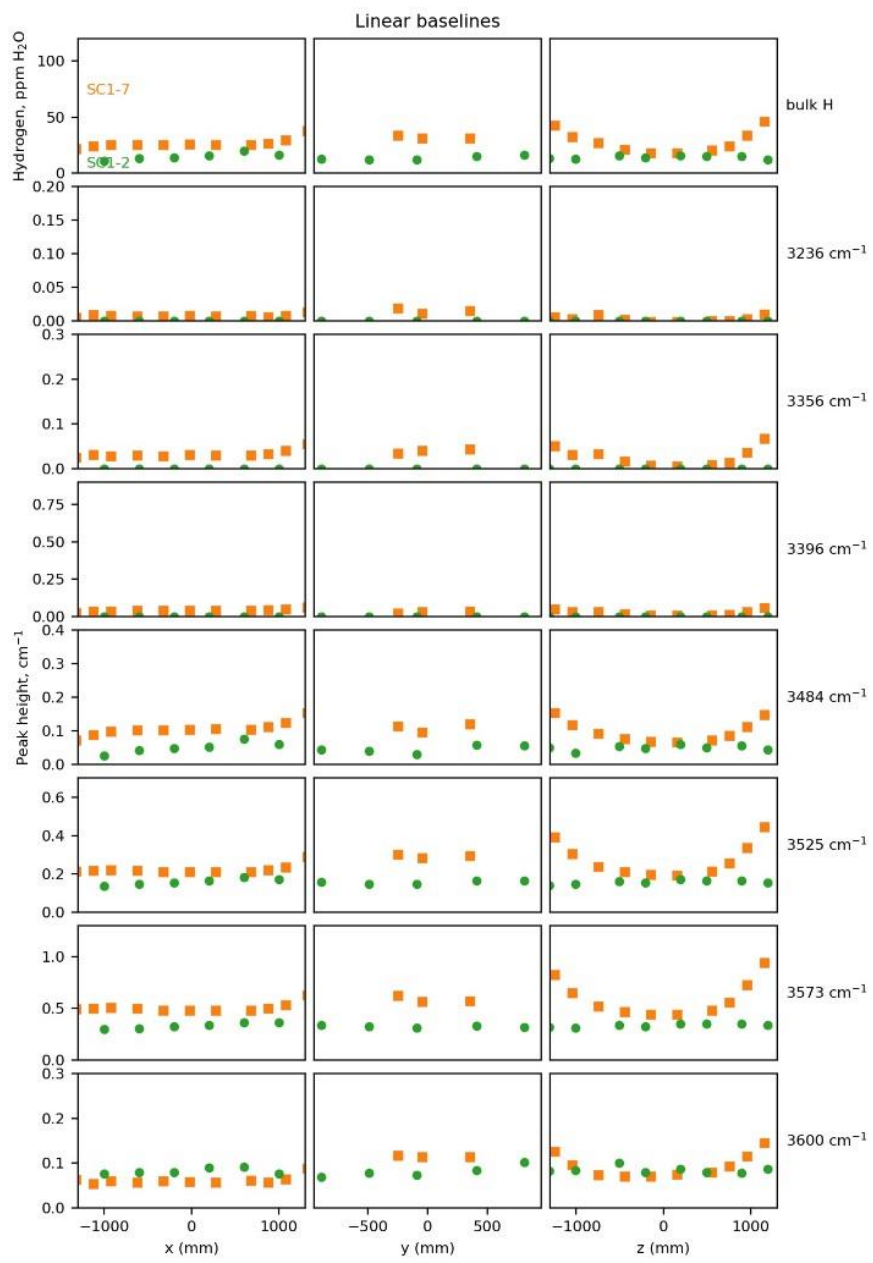


Figure 8. Bulk and site-specific hydrogen profiles relative to the initial measurements in Kilauea Iki olivine following heat treatment at 800°C, 1 atm, and fO₂ of QFM-2.

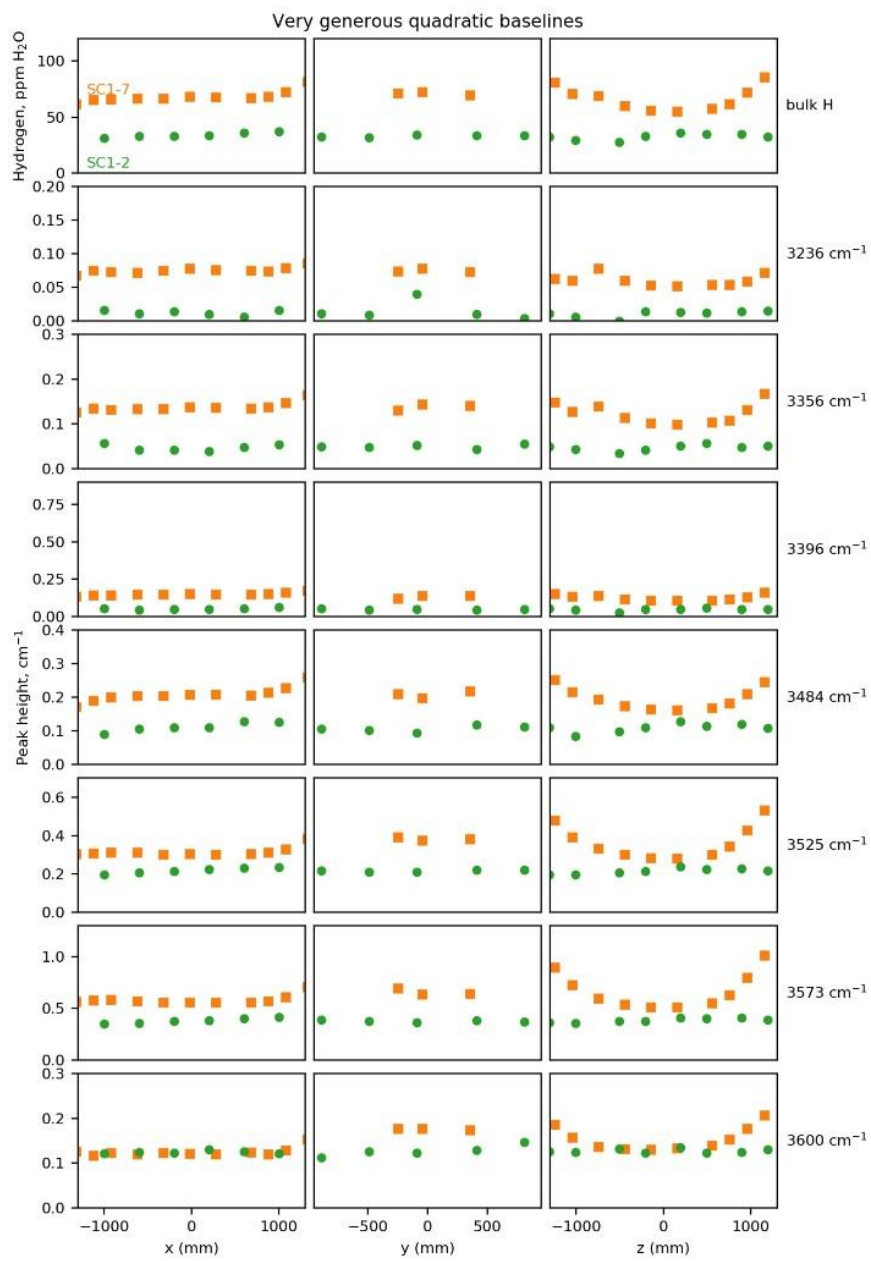
Supplementary Figures



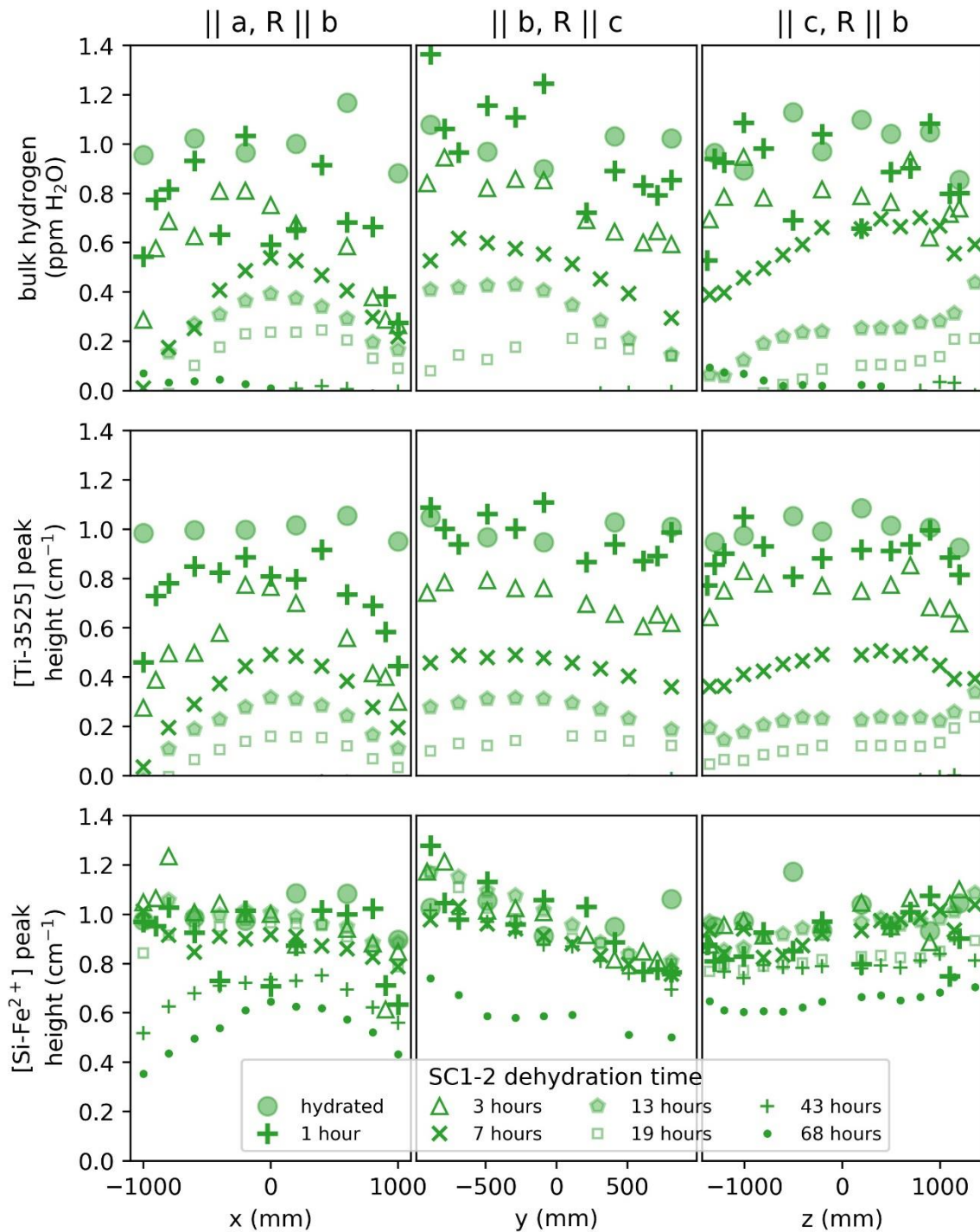
Supplementary Figure 1. Additional hydration profiles using the same quadratic baselines used for the hydration profiles in Figure 4. Hydration profiles from Figure 4 are included for comparison.



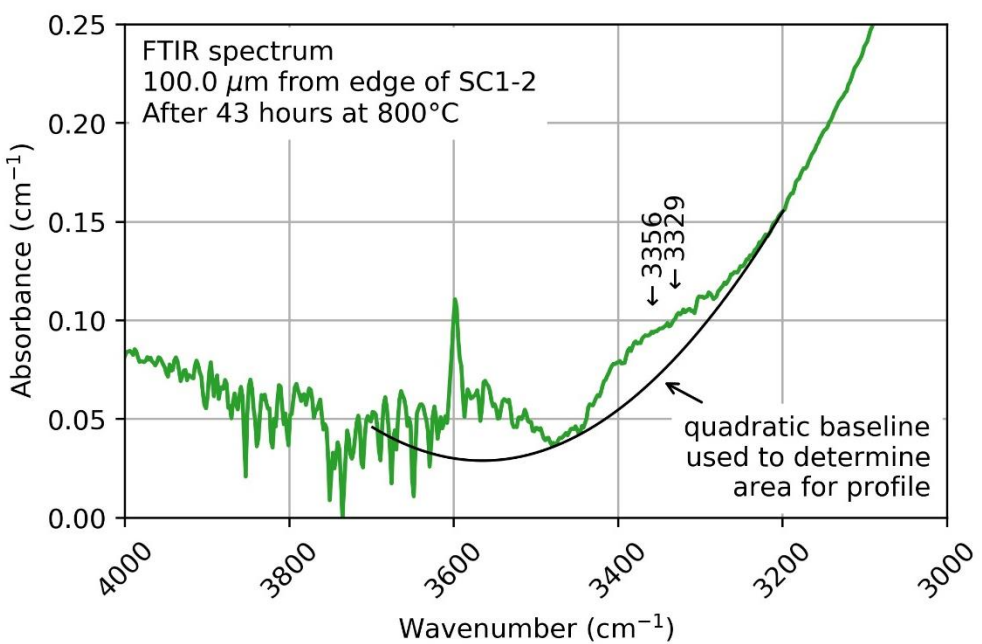
Supplementary Figure 2. Hydration profiles generated using linear baselines.



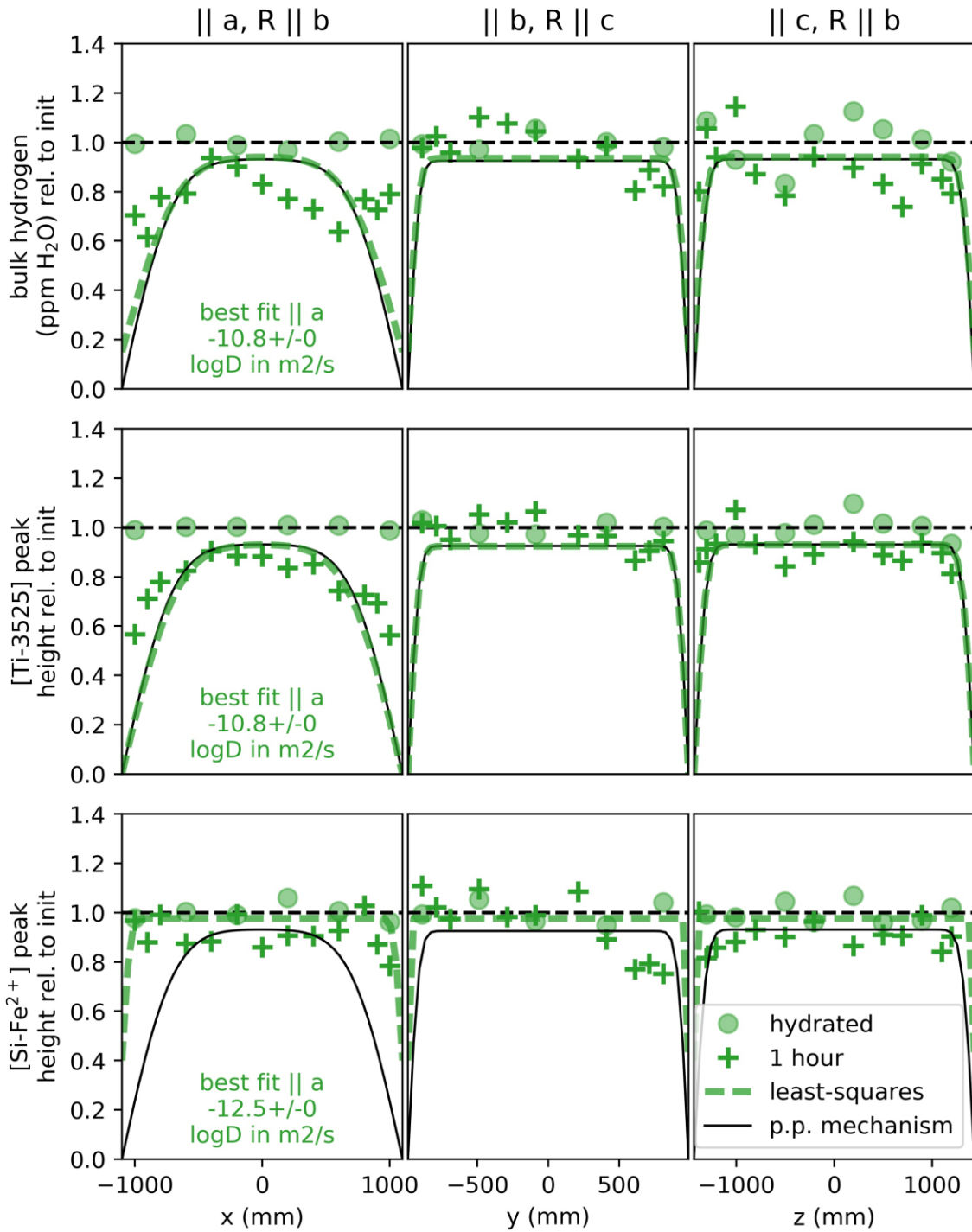
Supplementary Figure 3. Hydration profiles generated using quadratic baselines that are more generous than those shown in Figure 3.



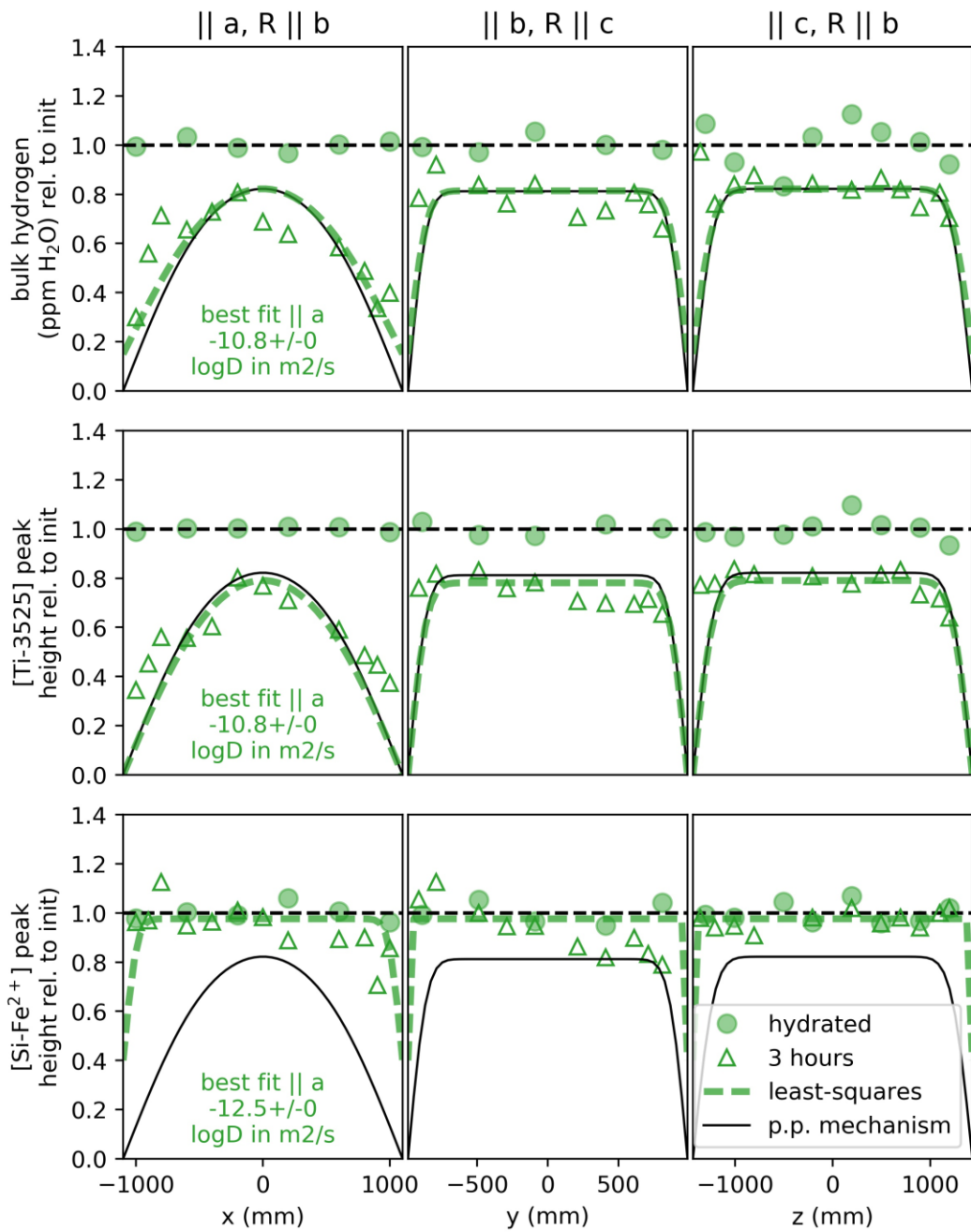
Supplementary Figure 4. Dehydration profiles for SC1-2 shown in Figure 7 generated using linear baselines like those shown in Figure 2. These linear baselines produce more symmetric profiles than the quadratic baselines used for modeling but often result in negative areas for spectra measured after the final two dehydration steps.



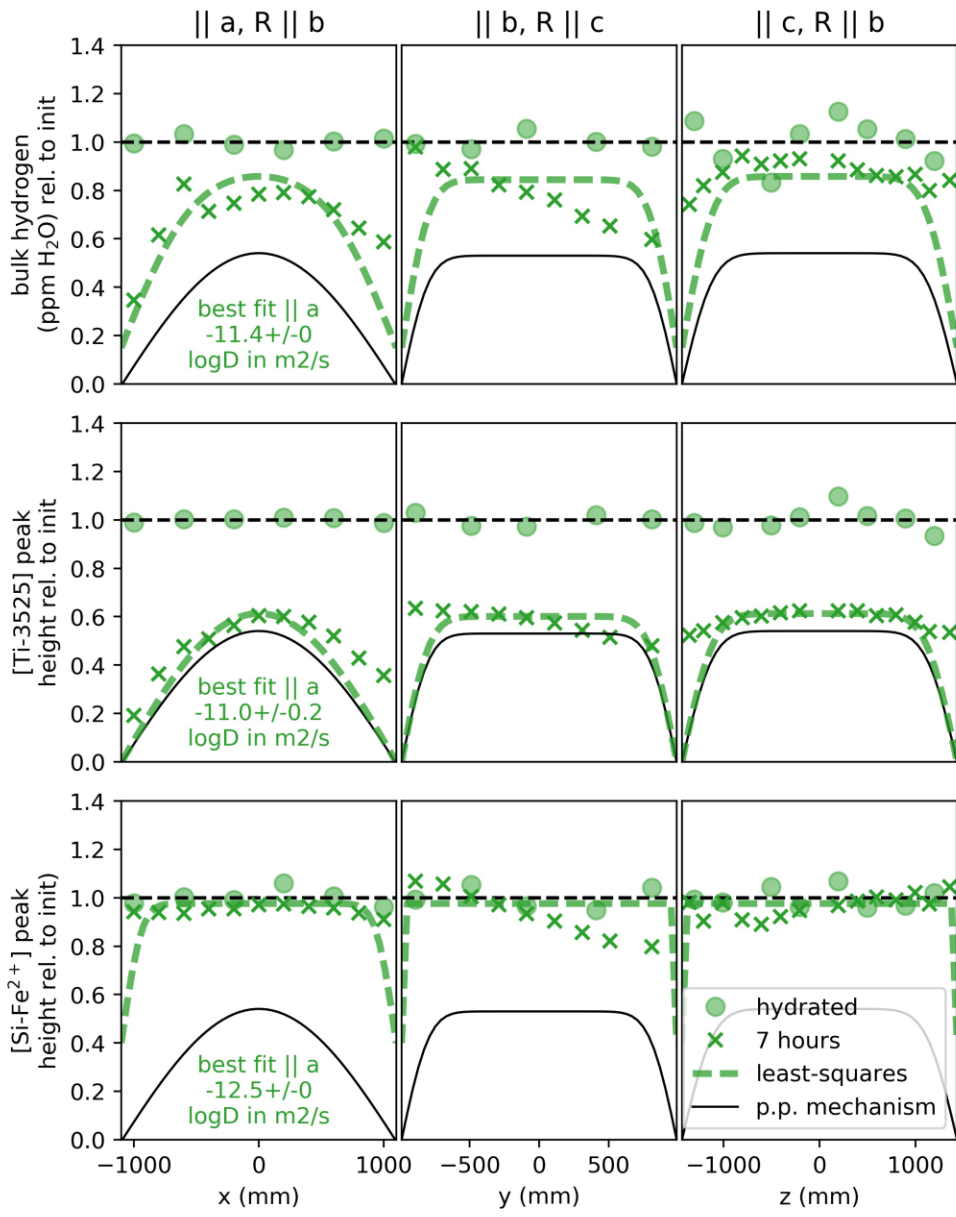
Supplementary Figure 5. One example of an FTIR spectrum measured near the edge of San Carlos olivine SC1-2 for which [tri] peaks (labeled) are observed and the baseline is strongly curved.



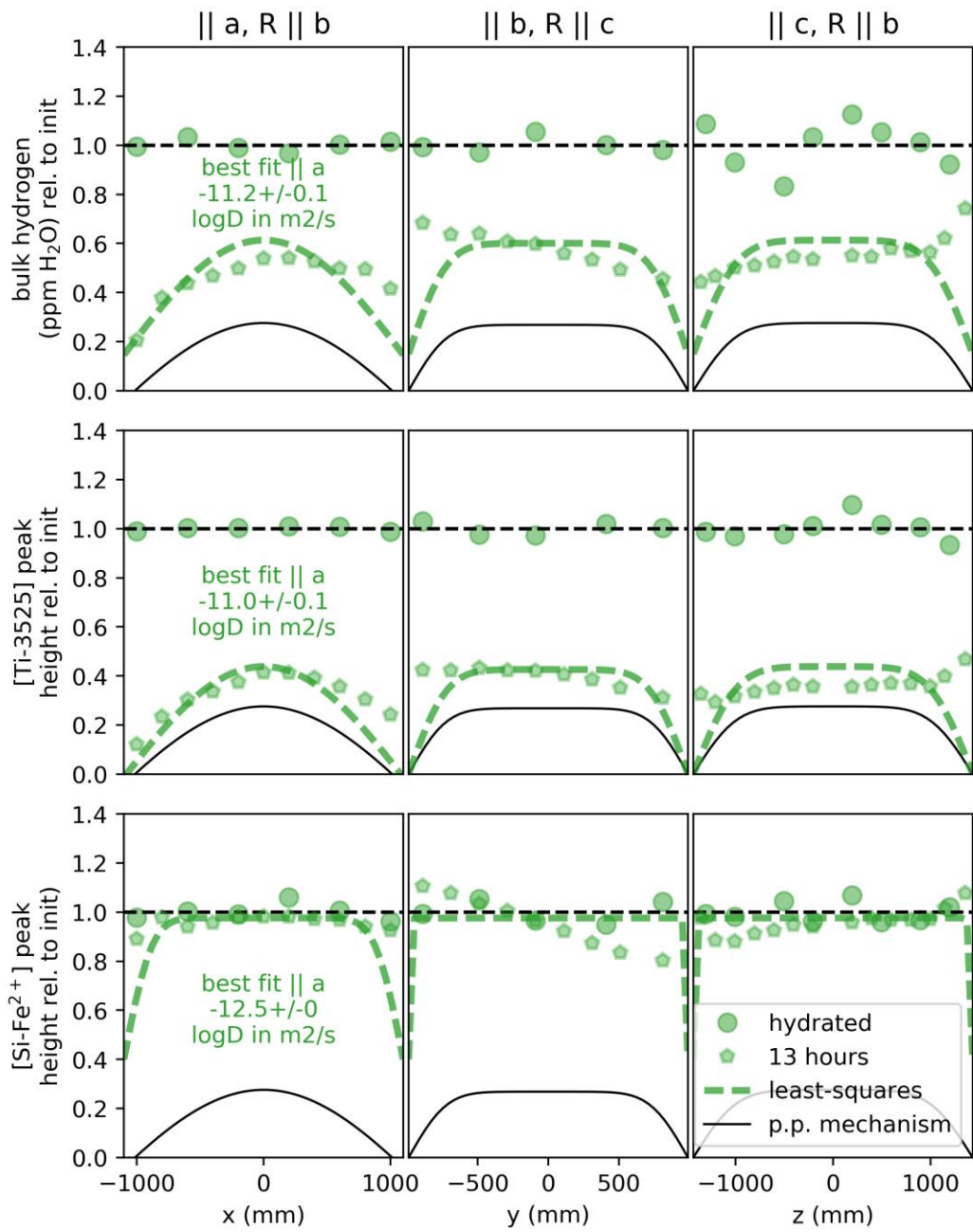
Supplementary Figure 6. Measured dehydration curves in the uncut San Carlos olivine SC1-2 after the first heating step shown in Figure 7 and modeled diffusion curves. The black 'p.p.' curves show the expected profiles if diffusion proceeds according to the proton-polaron mechanism as described by Kohlstedt and Mackwell (1998). The dashed green curves show the least-squares best-fit diffusion curves when the diffusivity was allowed to deviate from p.p. || [100].



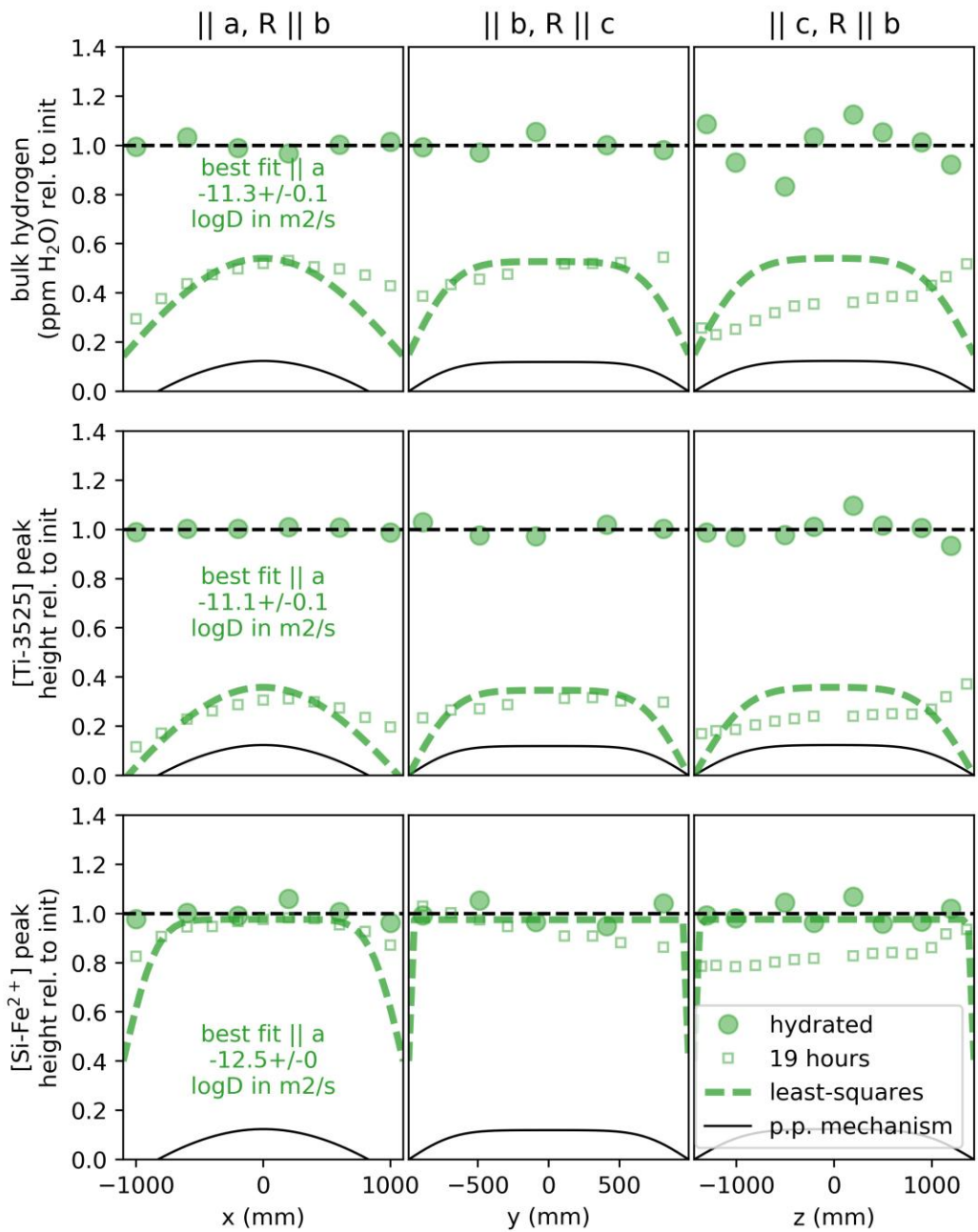
Supplementary Figure 7. Measured dehydration curves in the uncut San Carlos olivine SC1-2 after the second heating step shown in Figure 7 and modeled diffusion curves. The black 'p.p.' curves show the expected profiles if diffusion proceeds according to the proton-polaron mechanism as described by Kohlstedt and Mackwell (1998). The dashed green curves show the least-squares best-fit diffusion curves when the diffusivity was allowed to deviate from p.p. || [100].



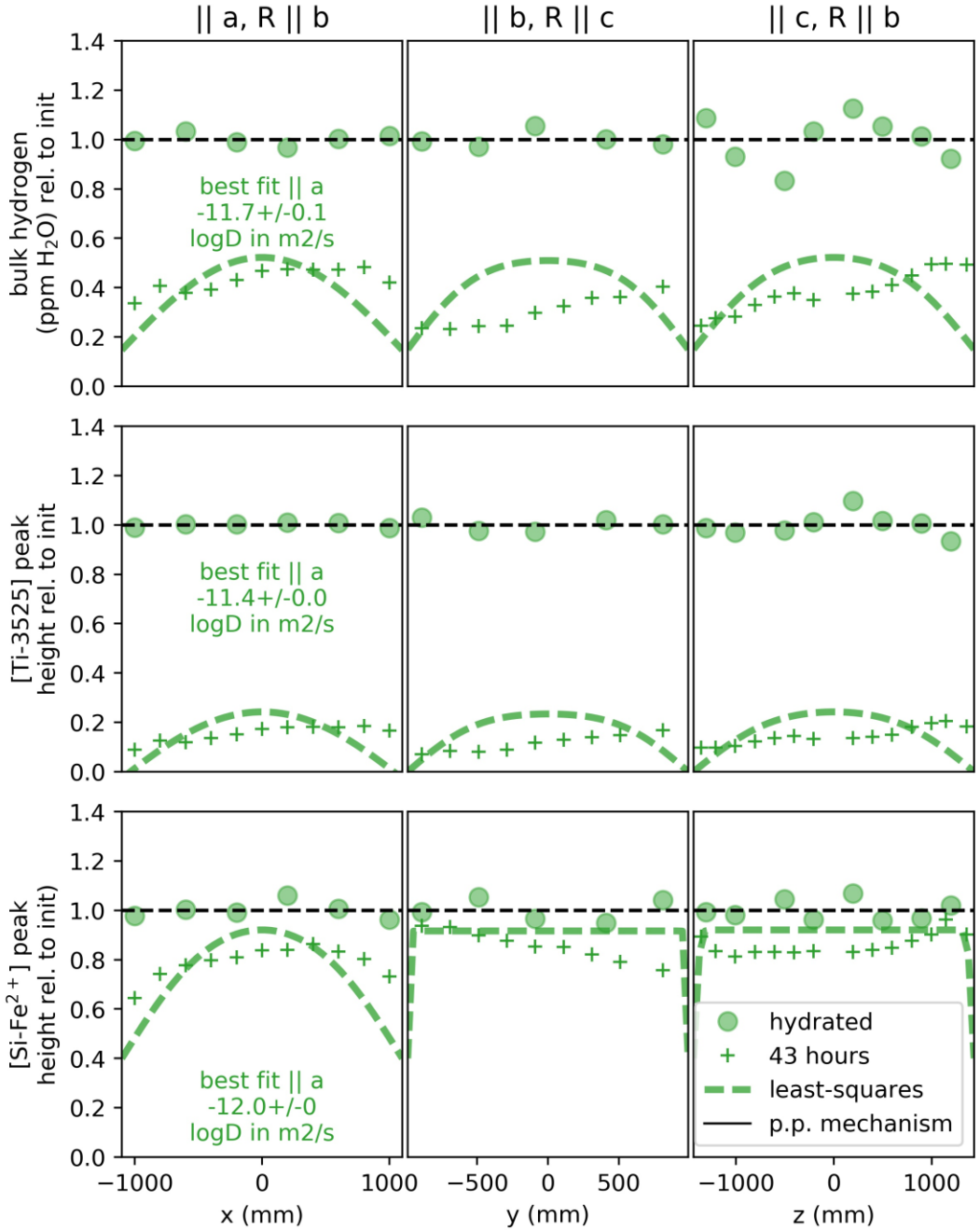
Supplementary Figure 8. Measured dehydration curves in the uncut San Carlos olivine SC1-2 after the third heating step shown in Figure 7 and modeled diffusion curves. The black 'p.p.' curves show the expected profiles if diffusion proceeds according to the proton-polaron mechanism as described by Kohlstedt and Mackwell (1998). The dashed green curves show the least-squares best-fit diffusion curves when the diffusivity was allowed to deviate from p.p. || [100] for [Ti]. The best-fit curve shown for [Si] is a maximum estimate assuming a final [Si] level of 0.4 times the initial hydrated state, and the best-fit curve shown for bulk H is a visual estimate. The least-squares best-fit to the bulk H data, $10^{-12.7 \pm 2.1} \text{ m}^2/\text{s}$, is lower but has a very large error that includes the visually estimated diffusivity of $10^{-11.5} \text{ m}^2/\text{s}$.



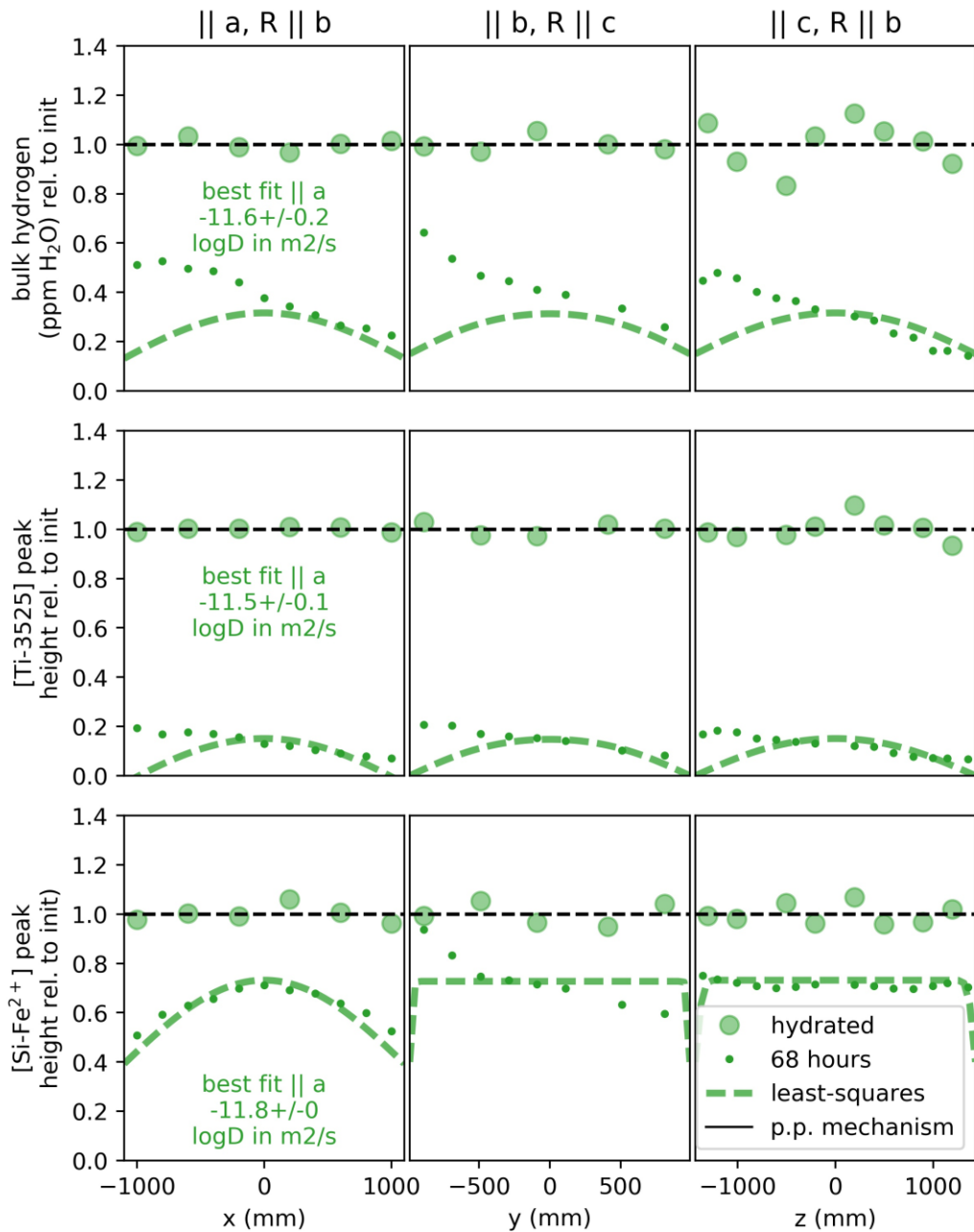
Supplementary Figure 9. Measured dehydration curves in the uncut San Carlos olivine SC1-2 after the fourth heating step shown in Figure 7 and modeled diffusion curves. The black ‘p.p.’ curves show the expected profiles if diffusion proceeds according to the proton-polaron mechanism as described by Kohlstedt and Mackwell (1998). The dashed green curves show the least-squares best-fit diffusion curves when the diffusivity was allowed to deviate from p.p. || [100] for bulk H and [Ti]. The best-fit curve shown for [Si] is a maximum estimate assuming a final [Si] level of 0.4 times the initial hydrated state.



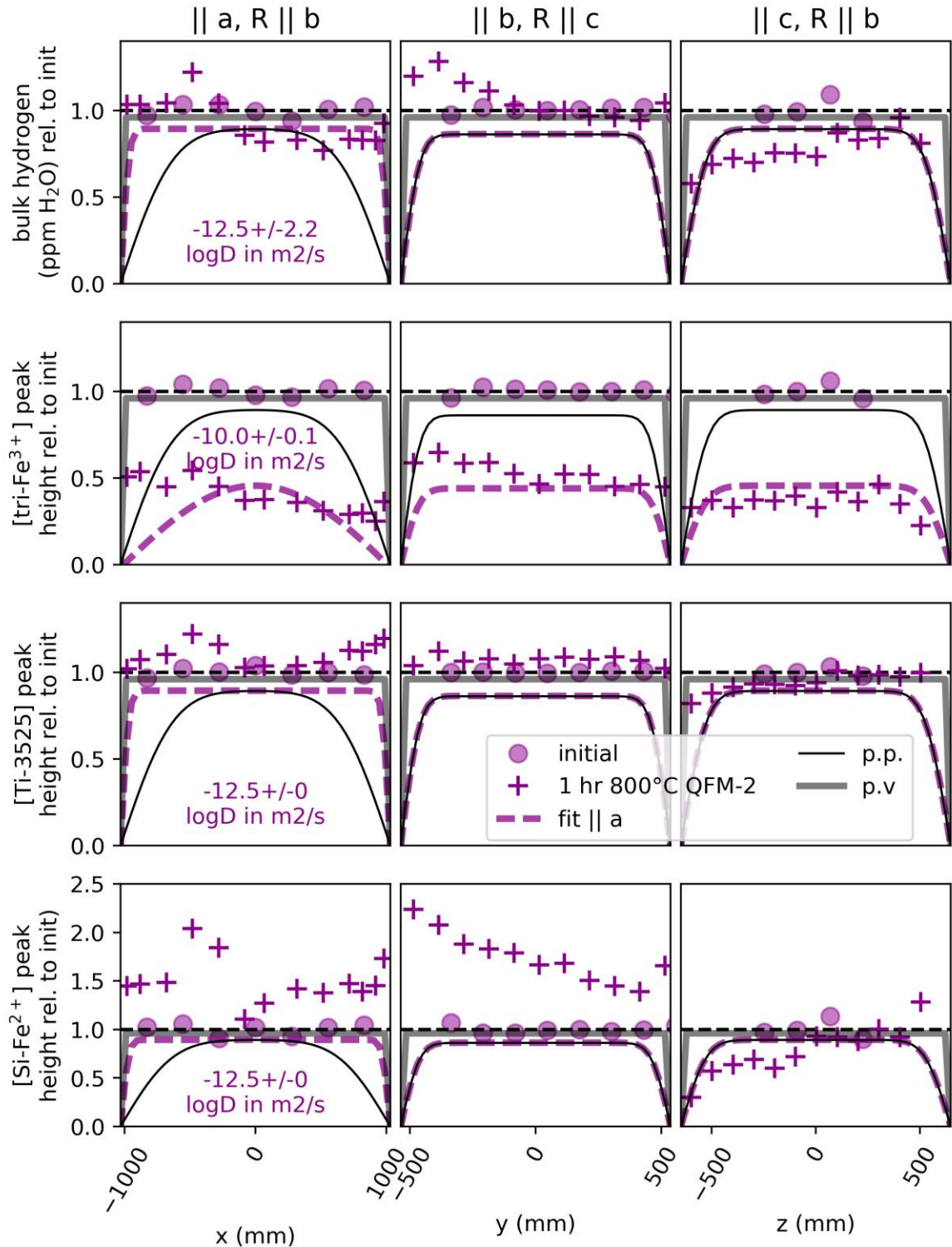
Supplementary Figure 10. Measured dehydration curves in the uncut San Carlos olivine SC1-2 after the fifth heating step shown in Figure 7 and modeled diffusion curves. The black 'p.p.' curves show the expected profiles if diffusion proceeds according to the proton-polaron mechanism as described by Kohlstedt and Mackwell (1998). The dashed green curves show the least-squares best-fit diffusion curves when the diffusivity was allowed to deviate from p.p. || [100] for bulk H and [Ti]. The best-fit curve shown for [Si] is a maximum estimate assuming a final [Si] level of 0.4 times the initial hydrated state and a fast direction || [100].



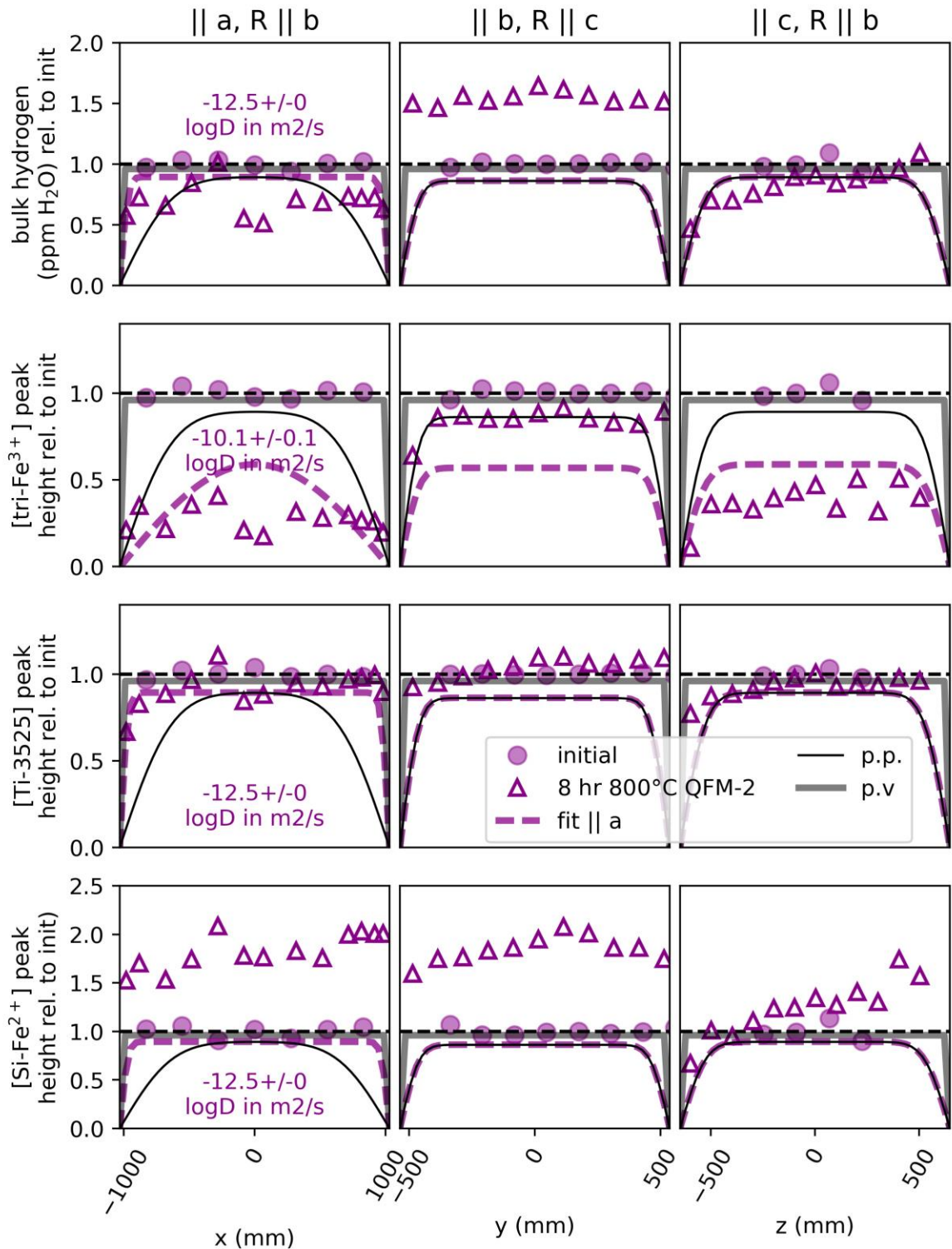
Supplementary Figure 11. Measured dehydration curves in the uncut San Carlos olivine SC1-2 after the sixth heating step shown in Figure 7 and modeled diffusion curves. Diffusion taking place entirely by the proton-polaron ‘p.p.’ mechanism as described by Kohlstedt and Mackwell (1998) would result in zero remaining H at this stage. The dashed green curves show the least-squares best-fit diffusion curves when the diffusivity was allowed to deviate from p.p. $\parallel [100]$ for bulk H and [Ti]. The best-fit curve shown for [Si] is a maximum estimate assuming a final [Si] level of 0.4 times the initial hydrated state and a fast direction $\parallel [100]$.



Supplementary Figure 12. Measured dehydration curves in the uncut San Carlos olivine SC1-2 after the seventh and final heating step shown in Figure 7 and modeled diffusion curves. Diffusion taking place entirely by the proton-polaron ‘p.p.’ mechanism as described by Kohlstedt and Mackwell (1998) would result in zero remaining H at this stage. The dashed green curves show the least-squares best-fit diffusion curves when the diffusivity was allowed to deviate from p.p. $\parallel [100]$ for bulk H and [Ti]. The best-fit curve shown for [Si] is a maximum estimate assuming a final [Si] level of 0.4 times the initial hydrated state and a fast direction $\parallel [100]$.



Supplementary Figure 13. Measured H profiles in the uncut Kilauea Iki olivine after the first heating step shown in Figure 8 and modeled diffusion curves. The dashed green curves show the least-squares best-fit diffusion curves when the diffusivity was allowed to deviate from p.p. || [100] for [tri-Fe³⁺]. The best-fit curves shown for bulk H, [Ti], and [Si] are maximum estimates of the diffusivities.



Supplementary Figure 14. Measured H profiles in the uncut Kilauea Iki olivine after the second heating step shown in Figure 8 and modeled diffusion curves. The dashed green curves show the least-squares best-fit diffusion curves when the diffusivity was allowed to deviate from p.p. || [100] for [tri-Fe³⁺]. The best-fit curves shown for bulk H, [Ti], and [Si] are maximum estimates of the diffusivities.

Bibliography

- Bell, D. R., and G. R. Rossman
1992 Water in Earth's Mantle: The Role of Nominally Anhydrous Minerals. *Science* 255(5050). WOS:A1992HH74400043: 1391–1397.
- Bell, D. R., G. R. Rossman, J. Maldener, D. Endisch, and F. Rauch
2003 Hydroxide in Olivine: A Quantitative Determination of the Absolute Amount and Calibration of the IR Spectrum. *Journal of Geophysical Research-Solid Earth* 108(B2). WOS:000181985400002. ://WOS:000181985400002.
- Berry, A. J., J. Hermann, H. S. C. O'Neill, and G. J. Foran
2005 Fingerprinting the Water Site in Mantle Olivine. *Geology* 33(11). WOS:000233059000008: 869–872.
- Berry, A. J., A. M. Walker, J. Hermann, et al.
2007 Titanium Substitution Mechanisms in Forsterite. *Chemical Geology* 242(1–2). WOS:000248433400010: 176–186.
- Blanchard, Marc, Jannick Ingrin, Etienne Balan, István Kovács, and Anthony C. Withers
2017 Effect of Iron and Trivalent Cations on OH Defects in Olivine. *American Mineralogist* 102(2): 302–311.
- Demouchy, S., and S. Mackwell
2006 Mechanisms of Hydrogen Incorporation and Diffusion in Iron-Bearing Olivine. *Physics and Chemistry of Minerals* 33(5). WOS:000240439000005: 347–355.
- Faul, Ulrich H., Christopher J. Cline II, Emmanuel C. David, Andrew J. Berry, and Ian Jackson
2016 Titanium-Hydroxyl Defect-Controlled Rheology of the Earth's Upper Mantle. *Earth and Planetary Science Letters* 452: 227–237.
- Ferguson, David J., Helge M. Gonnermann, Philipp Ruprecht, et al.
2016 Magma Decompression Rates during Explosive Eruptions of Kīlauea Volcano, Hawaii, Recorded by Melt Embayments. *Bulletin of Volcanology* 78(10): 71.
- Ferriss, E.
2015 Pynams: A Python Package for Interpreting FTIR Spectra of Nominally Anhydrous Minerals (NAMs). New York. <https://github.com/EFerriss/pynams>.
- Ferriss, E., T. Plank, D. Walker, and M. Nettles
2015 The Whole-Block Approach to Measuring Hydrogen Diffusivity in Nominally Anhydrous Minerals. *American Mineralogist* 100(4). WOS:000352175700017: 837–851.
- Ferriss, Elizabeth, Terry Plank, and David Walker
2016 Site-Specific Hydrogen Diffusion Rates during Clinopyroxene Dehydration. *Contributions to Mineralogy and Petrology* 171(6): 1–24.

Ingrin, J., J. Liu, C. Depecker, et al.

2013 Low-Temperature Evolution of OH Bands in Synthetic Forsterite, Implication for the Nature of H Defects at High Pressure. *Physics and Chemistry of Minerals* 40(6). WOS:000319771000005: 499–510.

Jollands, Michael C., José Alberto Padrón-Navarta, Jörg Hermann, and Hugh St.C. O'Neill

2016 Hydrogen Diffusion in Ti-Doped Forsterite and the Preservation of Metastable Point Defects. *American Mineralogist* 101(7): 1560–1570.

Keppler, Hans, and Joseph R. Smyth

2006 Water in Nominally Anhydrous Minerals, vol.62. *Reviews in Mineralogy and Geochemistry*. Mineralogical Society of America.

Kohlstedt, D. L., and S. J. Mackwell

1998 Diffusion of Hydrogen and Intrinsic Point Defects in Olivine. *Zeitschrift Fur Physikalische Chemie-International Journal of Research in Physical Chemistry & Chemical Physics* 207. WOS:000076569300010: 147–162.

Kurosawa, M., H. Yurimoto, and S. Sueo

1997 Patterns in the Hydrogen and Trace Element Compositions of Mantle Olivines. *Physics and Chemistry of Glasses* 24: 385–395.

Libowitzky, E., and G. R. Rossman

1996 Principles of Quantitative Absorbance Measurements in Anisotropic Crystals. *Physics and Chemistry of Minerals* 23(6). WOS:A1996VD85000001: 319–327.

Mackwell, S. J., and D. L. Kohlstedt

1990 Diffusion of Hydrogen in Olivine - Implications for Water in the Mantle. *Journal of Geophysical Research-Solid Earth and Planets* 95(B4). WOS:A1990CZ37500052: 5079–5088.

Mosenfelder, J. L., N. I. Deligne, P. D. Asimow, and G. R. Rossman

2006 Hydrogen Incorporation in Olivine from 2–12 GPa. *American Mineralogist* 91(2–3). WOS:000235472000007: 285–294.

Padrón-Navarta, Jose Alberto, Joerg Hermann, and Hugh St. C. O'Neill

2014 Site-Specific Hydrogen Diffusion Rates in Forsterite. *Earth and Planetary Science Letters* 392: 100–112.

Peslier, A. H., and J. F. Luhr

2006 Hydrogen Loss from Olivines in Mantle Xenoliths from Simcoe (USA) and Mexico: Mafic Alkalic Magma Ascent Rates and Water Budget of the Sub-Continental Lithosphere. *Earth and Planetary Science Letters* 242(3–4). WOS:000235855100006: 302–319.

Ruprecht, Philipp, and Terry Plank

2013 Feeding Andesitic Eruptions with a High-Speed Connection from the Mantle. *Nature* 500(7460): 68–72.

Shuai, Kang, and Xiaozhi Yang

2017 Quantitative Analysis of H-Species in Anisotropic Minerals by Polarized Infrared Spectroscopy along Three Orthogonal Directions. Contributions to Mineralogy and Petrology 172(2–3): 14.

Withers, A. C.

2013 The Pitzer and Stern Equation of State for Water.

<http://www.geo.umn.edu/people/researchers/withe012/fugacity.htm>, accessed August 6, 2013.

Withers, Anthony C, Hélène Bureau, Caroline Raepsaet, and Marc M Hirschmann

2012 Calibration of Infrared Spectroscopy by Elastic Recoil Detection Analysis of H in Synthetic Olivine. Chemical Geology 334: 92–98.